Centro Federal de Educação Tecnológica de
Minas Gerais - CEFET/MG
Graduate Program in
Mathematical and Computational Modeling

Thesis

Computational Investigation of CO_2 Reduction Intermediates on Doped and Stepped Silver Surfaces

Marionir Macedo Castelo Branco Neto

PhD thesis presented for the Mathematical and Computational Modeling program of Centro Federal de Educação Tecnológica de Minas Gerais.
Supervisor: Breno Rodrigues Lamaghere Galvão (Centro Federal de Educação Tecnológica de Minas Gerais)
Co-supervisor: Juarez Lopes Ferreira da Silva (Universidade de São Paulo)

May 12, 2025

Branco Neto, Marionir Macedo Castelo
B816c Computational investigation of CO_2 reduction intermediates on doped and stepped silver surfaces / Marionir Macedo Castelo Branco Neto. – 2024.
ix, 57 f.

Tese de doutorado apresentada ao Programa de Pós-Graduação em Modelagem Matemática e Computacional.
Orientador: Breno Rodrigues Lamaghere Galvão.
Coorientador: Juarez Lopes Ferreira da Silva.
Tese (doutorado) – Centro Federal de Educação Tecnológica de Minas Gerais.

1. Superfícies (Tecnologia) – Teses. 2. Química quântica – Matemática – Teses. 3. Hidrogênio – Simulação computacional – Teses. 4. Eletrólise – Simulação computacional – Teses. I. Galvão, Breno Rodrigues Lamaghere. II. Silva, Juarez Lopes Ferreira da. III. Centro Federal de Educação Tecnológica de Minas Gerais. IV. Título.

CDD 519.233

Elaboração da ficha catalográfica pela bibliotecária Jane Marangon Duarte, CRB 6ª 1592 / Cefet/MG

SERVIÇO PÚBLICO FEDERAL
MINISTÉRIO DA EDUCAÇÃO
CENTRO FEDERAL DE EDUCAÇÃO TECNOLÓGICA DE MINAS GERAIS
COORDENAÇÃO DO PROGRAMA DE PÓS-GRADUAÇÃO EM MODELAGEM MATEMÁTICA E COMPUTACIONAL

"COMPUTATIONAL INVESTIGATION OF CO2 REDUCTION INTERMEDIATES ON DOPED AND STEPPED SILVER SURFACES".

Tese de Doutorado apresentada por **Marionir Macedo Castelo Branco Neto**, em 28 de junho de 2024, ao Programa de Pós-Graduação em Modelagem Matemática e Computacional do CEFET-MG, e aprovada pela banca examinadora constituída pelos professores:

Prof. Dr. Breno Rodrigues Lamaghere Galvão
Centro Federal de Educação Tecnológica de Minas Gerais

Prof. Dr. Guilherme Ferreira de Lima
Universidade Federal de Minas Gerais

Prof. Dr. Hélio Anderson Duarte
Universidade Federal de Minas Gerais

Prof. Dr. Thiago Gomes de Mattos
Centro Federal de Educação Tecnológica de Minas Gerais

Prof. Dr. José Luiz Acebal Fernandes
Centro Federal de Educação Tecnológica de Minas Gerais

Visto e permitida a impressão.

Prof. Dr. Thiago de Souza Rodrigues
Coordenador do Programa de Pós-Graduação Stricto Sensu em Modelagem Matemática e Computacional

Acknowledgment

I am deeply grateful to Professor Breno R. L. Galvão and Professor Juarez L. F. Da Silva for their guidance and support, to Doctor Lucas G. Verga for his invaluable contribution to the research project, and to the members of the Quitrem and QTNano groups. Also, to FAPEMIG (grant APQ-00597-22) and the employees of CEFET-MG. Lastly, but not least, I extend my gratitude to my family for their unwavering support.

Resumo

Muitos processos químicos importantes se beneficiam dos avanços em catalisadores heterogêneos, especialmente aqueles que são catalisados por superfícies metálicas, que muitas vezes são influenciados por imperfeições, como degraus e dopantes. Na primeira parte deste trabalho, foi investigado o impacto da dopagem com um único dopante Rh no comportamento de adsorção de OH e CO em superfícies de Ag(211) com degraus, usando cálculos de teoria do funcional da densidade (DFT) com correção de van der Waals. A estabilidade do dopante Rh na superfície é maior em sítios com alta coordenação, mas, quando as moléculas estão presentes, os sítios menos coordenados são favorecidos. Essa mudança é atribuída à redistribuição de carga induzida pelo dopante e a um pico distinto na densidade de estados. Moléculas próximas ao dopante podem modificar a distribuição de carga local e afetar as interações entre dopante e superfície. Isso pode deslocar o dopante para favorecer locais de adsorção menos coordenados em comparação com a superfície sem moléculas. O OH se adsorve fortemente em superfícies de prata, e sua ligação é mais forte com o dopante de Rh devido à diferença de eletronegatividade entre eles. Em contraste, o CO se adsorve fisicamente na superfície não dopada, mas se adsorve quimicamente em superfícies dopadas. Na segunda fase do estudo, foi investigado o processo de redução de CO_2 usando o método computacional do eletrodo de hidrogênio (CHE), analisando superfícies de Ag(211) limpas e dopadas com um único átomo de Fe, Co, Ni, Cu, Rh ou Ir. Também avaliamos se os materiais propostos são suscetíveis a envenenamento por OH ou favorecem a reação de evolução de hidrogênio (HER), reação competidora. Nossos cálculos revelaram uma fraca mistura de densidade eletrônica entre o hospedeiro e o dopante, caracterizada por picos agudos na densidade de estados próximos à energia de Fermi, exceto no caso de dopantes de cobre. A energia de adsorção de intermediários varia entre diferentes substratos, levando a perfis de reação únicos. Superfícies com o dopante cobre tendem a desorver espontaneamente CO, ao contrário de outros elementos do quarto período (Fe, Co, Ni) que se ligam ao CO e podem favorecer a HER. Em contraste, os dopantes Ir e Rh são eletrocatalisadores promissores, favorecendo a redução de CO e suprimindo a HER em potenciais mais baixos que o cobre. Além disso, eles não são propensos a envenenamento por radicais OH.

Palavras-chave: Superfícies com degraus, cálculos *ab initio*, Modelo computacional do Eletrodo de Hidrogênio

Abstract

Many significant chemical processes benefit from advancements in heterogeneous catalysts, particularly those catalyzed by metallic surfaces, which are often influenced by imperfections like kinks and dopants. In our study, we first investigated the impact of single-atom Rh dopants on the adsorption behavior of OH and CO on stepped Ag(211) surfaces using density functional theory calculations with van der Waals correction. The stability of Rh dopant on the surface is highest at highly-coordinated sites, but when both molecules are present, the least coordinated site is favored. This shift is attributed to dopant-induced charge redistribution and a distinct peak in the density of states. Molecules near the dopant can modify the local charge distribution and affect dopant-surface interactions. This may shift the dopant to favor less coordinated adsorption sites compared to the surface without molecules. OH strongly chemisorbs to silver surfaces, and its bond is stronger with Rh dopant due to their electronegativity difference. In contrast, CO physisorbs on non-doped silver but chemisorbs with single-atom Rh dopants. In the second phase of our study, we investigated the reduction process of CO_2 using the computational hydrogen electrode (CHE) method, analyzing clean and Fe, Co, Ni, Cu, Rh and Ir single-atom doped Ag(211) surfaces. We also assessed whether the proposed materials are susceptible to OH poisoning or enhance the competing HER reaction (HER). Our calculations revealed weak electronic density mixing between the host and dopant, characterized by sharp peaks in the density of states near the Fermi energy, except in the case of copper-doped SAAs. The adsorption energy of intermediates varies across different substrates, leading to unique reaction profiles. Copper-doped SAAs tend to spontaneously desorb CO, unlike other fourth-period elements (Fe, Co, Ni) that bind to CO and may enhance the HER. In contrast, Ir and Rh dopants are promising electrocatalysts, favoring CO reduction and suppressing the HER at lower potentials than copper. Moreover, they are not prone to poisoning by OH radicals.

Keywords: Stepped surfaces, *ab initio* calculations, Computational Hydrogen Electrode Model

Contents

Figure List ix

1 Introduction 1
- 1.1 Problem Characterization . . . 1
- 1.2 Justification . . . 3
- 1.3 Objectives . . . 3
  - 1.3.1 General Objectives . . . 3
  - 1.3.2 Specific Objectives . . . 4

I Theoretical Background 5

2 Quantum Chemistry 6
- 2.1 Schröndiger Equation on Many Body Problem . . . 6
  - 2.1.1 Born–Oppenheimer Approximation . . . 7
- 2.2 Density Functional Theory . . . 11
  - 2.2.1 Introduction . . . 11
  - 2.2.2 Hohenberg-Kohn Theorems . . . 12
  - 2.2.3 Kohn-Sham Equations . . . 14
  - 2.2.4 Exchange–Correlation Functionals . . . 16
- 2.3 Computational Hydrogen Electrode Model . . . 17
- 2.4 CO_2 Reduction Reaction . . . 18

3 Computational Details 20
- 3.1 Computational Methodology . . . 20
- 3.2 Adsorption on Stepped Surfaces . . . 21
- 3.3 Geometric Parameters . . . 24
  - 3.3.1 Effective Coordination Number . . . 24
- 3.4 Energetic Parameters . . . 25

3.5 Electronic Parameters 25

II Results and Conclusions **27**

4 Single-atom Rh-dopant Effects on the Adsorption Properties of Stepped Ag(211) Surfaces **28**
4.1 Clean and Doped Surface 28
4.2 Adsorption Properties 30
4.2.1 Geometric Parameters 34
4.2.2 Work function Change and Electron Density Difference 35

5 Computational Screening of Silver-based Single-atom Alloys Catalysts for CO_2 Reduction **38**
5.1 TM@Ag(211) Surfaces 38
5.2 Adsorption of CO_2RR Intermediates 41
5.3 Screening of TM/Ag(211) Single-atom Alloy Catalyst for CO_2RR 45

6 Conclusion **48**

Bibliography **50**

List of Figures

2.1 PES of diatomic system. 8
2.2 Complite possible reaction pathways for reducing CO_2 to CO, HCOOH, CH_3OH, and CH_4 involve a sequence of PCET. 18
2.3 Steps CO_2RR and HER given by pathway green and red, respectively. The blue platform represents the substrate Ag(211). Reproduced from [1], with the permission of AIP Publishing. 19

3.1 Representation of the Ag(211) surface: a) Illustration showing the intersection of step and terrace planes. b) Identification of potential dopant positions. c) Side view and d) top view of the Ag(211) surface, with atoms exposed to the vacuum colored based on their effective coordination number values. Adsorption sites are categorized into several groups: top (T1, T2, and T3), bridge (B1, B2, B3, B4, and B5), hollow hcp (H1, H2), and hollow fcc (F1, F2) sites. These two last forms differ from each other in their packing factor. Reproduced from Ref. [2] with permission from the Royal Society of Chemistry. 23

4.1 Bader charges for the Ag atoms in the doped surfaces. Q_{eff} gradient bar refers to Ag atoms only, while the Rh charges are given in the numbers in blue. e is the elementary charge, with a value of 1.6×10^{-19} coulomb. Reproduced from Ref. [2] with permission from the Royal Society of Chemistry. 30
4.2 Local density of states (d-states contribution) for the non-doped and Rh-doped (step, terrace, and corner) Ag(211) surfaces. Comparing, the LDOS was calculated for the Rh and the replaced Ag atoms, respectively. The d-band centers are indicated by vertical lines, while the vertical dashed line at zero energy indicates the Fermi energy. Reproduced from Ref. [2] with permission from the Royal Society of Chemistry. 31

4.3 Top and side view of the adsorption configurations for OH and CO on Ag(211). The label above each structure represents the adsorption site. Ag is grey, O is red, C is brown and H is light pink. Reproduced from Ref. [2] with permission from the Royal Society of Chemistry. 32
4.4 Top and side view of the adsorption configurations for OH and CO on Ag(211) doped with Rh. The label above each structure represents the adsorption site followed by the chain in which the dopant lies. Rh is shown in green, Ag in grey, O in red C in brown and H in light pink. Reproduced from Ref. [2] with permission from the Royal Society of Chemistry. 33
4.5 Geometric parameters and adsorption energies for the a) OH/Rh@Ag(211) and b) CO/Rh@Ag(211) systems. The elements in parenthesis represent to which atoms of the doped surface the molecule is bound to. Reproduced from Ref. [2] with permission from the Royal Society of Chemistry. 34
4.6 Work function difference induced by the presence of the molecules on doped and non-doped surfaces for OH (left panel) and CO (right panel). Reproduced from Ref. [2] with permission from the Royal Society of Chemistry. 35
4.7 Electron density difference. (0.0014 eÅ^{-3}) for CO and OH adsorbed on Ag(211) doped with Rh. The label for the sites follows the ones defined in the text. Yellow and blue colors show accumulation and depletion of charge, respectively. Reproduced from Ref. [2] with permission from the Royal Society of Chemistry. 37

5.1 Local density of states along with the *d*-band center analyses for single-atoms at the step (solid line) or terrace positions (dashed). Blue curves correspond to the non-doped Ag(211) surface, while the remaining colors correspond to the doped surface. The *d*-band centers are indicated with colored vertical lines, while the Fermi energy is indicated by a vertical black dashed line. Reproduced from [1], with the permission of AIP Publishing. . 40
5.2 Top and side view of the lowest energy adsorption configurations on Ag(211). The adsorption energy is given eV. Ag is gray, O is red C is brown and H is light pink. Reproduced from [1], with the permission of AIP Publishing. 41
5.3 Top and side views for the minimum energy adsorption configuration of each system with the TM Dopant on the step position (left) and terrace position (right). Adsorption energy is given in parenthesis. Reproduced from [1], with the permission of AIP Publishing. 43
5.4 Free energies of formation (relative to a clean surface, and gas-phase H_2 and CO) between the adsorbed species. The lines represent the fitted data for each molecule separately. Reproduced from [1], with the permission of AIP Publishing. 45

5.5 Free energy diagrams for non-doped silver and SAA surfaces with dopants on the step (a) and terrace (b) positions. The free energy for the competing HER and formation of H_2O from adsorbed OH are given as sidebars. In the HER diagram, the solid lines indicate that the potential determining step is the hydrogen adsorption, rather than its subsequent hydrogenation and desorption as H_2, which is shown in dash. Reproduced from [1], with the permission of AIP Publishing. 46

1 Introduction

1.1 Problem Characterization

Carbon dioxide (CO_2) is a pollutant generated in several industrial applications, including large energy production plants such as thermometric, construction industry, food production and others. Evidence from research entities, such as the Intergovernmental Panel on Climate Change (2007), shows that human activities are largely responsible for global warming in the last 50 years, as it is understood that the emission of carbon dioxide is very high [3]. Once in excess, CO_2 hinders the dissipation of heat by absorbing infrared light. Undoubtedly, the presence of this carbon gas in the atmospheric air is vital for human beings, however, what currently occurs is the imbalance of the levels of this compound. Mainly due to the increase in fossil fuels, emission of CO_2 increased by 19 % in Brazil between 2008-2018. Considering this, it can be said that there is a need to develop new sustainable energy alternatives, associating technologies capable of capturing CO_2 and converting it into chemical products of high economic value [4, 5].

The depletion of non-renewable energy sources like fossil fuel, along with the ensuing environmental pollution from the combustion of such energy carriers, are two major challenges for human society in the twenty-first century due to rapidly rising energy consumption and demand. Therefore, the alternative that will be addressed in this work is the conversion of CO_2 into non-polluting substances with market value. This type of activity attracted great interest, and the electrolysis method has been generally considered one of the most promising solutions. The basis of what is known about the conversion of CO_2 into higher value-added products is comparable to the principles of photosynthesis, which is the mechanism used by plants to convert CO_2 and water into hydrocarbons [4]. There exists a reaction limit in natural processes that do not exceed an efficiency of 7% due to an energetic bottleneck along the reaction pathway [6].

The pressing urgency to tackle climate change and curb greenhouse gas emissions has underscored the critical importance of developing technologies for converting carbon dioxide (CO_2) into valuable chemicals and fuels. This approach not only helps mitigate CO_2 emissions but also offers a means to effectively store and utilize excess energy. For instance, by coupling clean and renewable energy sources like photovoltaic cells or wind

power with CO_2 conversion technologies, we can potentially transform harmful gases into valuable fuels. These fuels could then be used in situations where replacing hydrocarbon burning with intermittent clean sources is challenging. However, it is crucial to ensure that the captured CO_2 is not released back into the atmosphere but rather recaptured within the system and fed back into the conversion unit. This closed-loop process, known as the carbon cycle, offers a green solution without entirely abandoning combustion cells where they are indispensable. Notably, the conversion of CO_2 to fuels is a pivotal technology within this framework, with efficient CO_2 reduction being paramount.

One can cite several methods for CO_2 reduction. Among them are the thermochemical method [7], the photochemical method [8], homogeneous catalysis [9], and heterogeneous electrocatalysis. Electrochemical catalysis emerges as a particularly promising approach for the CO_2 reduction reaction (CO_2RR). There are several advantages of using this method compared to others, including ease of operation. Electrolysis allows for more straightforward control of the conversion process, as parameters such as electric current can be precisely adjusted. The flexibility in catalyst selection is also an advantage, as different types of catalysts can be utilized to optimize selectivity and efficiency. Of course, there are some disadvantages of this method compared to others. These include lower Faradaic efficiency, (how efficiently electrical current application is converted into electrochemical reaction products.), which may result in some waste of electrical energy. Nonetheless, this method is promising for study, as it is continuously advancing, yielding scientific progress and attracting financial investment [10].

Eletrocatalysts based on copper (Cu), gold (Au), and silver (Ag) present intriguing options for CO_2RR applications. While copper can yield a wide array of C_1 and C_2 products [11], gold and silver are renowned for their high Faradaic efficiencies in reducing CO_2 to carbon monoxide (CO) [12]. Various strategies can be employed to enhance the activity or selectivity of these monometallic catalysts, such as controlling nanoparticle size and shape [13], modifying supporting materials [14], and manipulating the microenvironment near the catalyst surface [15].

However, these strategies are often constrained by linear scaling relationships between the adsorption of key reaction intermediates, limiting the overall catalytic performance. For instance, the reduction of CO_2 to CO is often hindered by the adsorption energies of the hydrocarboxyl radical (COOH) and CO, while the relationship between hydrogenated carbon monoxide (COH or CHO) and CO governs the production of more reduced C1 products like methane (CH_4).

Recent advancements in single-atom dopant technology have offered a promising avenue to circumvent these linear scaling relationships and enhance catalyst performance for various chemical reactions [16]. Single-atom alloy catalysts (SAACs) activate adsorbed molecules strongly before spillover onto a noble metal surface, where selective catalysis and desorption occur. These SAACs have shown high Faradaic efficiency for CO_2 reduction, with the main product being CO [17]. However, achieving high-value products such as alcohols remains challenging.

1.2 Justification

Given the importance of the CO_2 reduction reaction, it is desirable to have a deep atomistic understanding of its intermediates and mechanisms, but this has not been achieved so far [18]. Computational methods offer ways to simulate electrocatalytic reactions effectively, and in recent times, computational methods have helped CO_2RR [19].

Our ability to create an efficient electrolytic cell is dependent on our knowledge about the intermediate stages of the reaction as well as the substrate used, the identification of adsorption sites, substrate design, and others. Rigorous computational simulations must be done to verify the best substrates that can be used as cathodes.

While the choice of the metal is very important in determining the products that can be obtained, the surface structure and exposed facet can also influence the reaction mechanisms and the overall catalyst activity [20, 21]. To simulate sites with lower coordination numbers that may be present on real surfaces, such as kinks and steps, one can consider high-Miller-index stepped surfaces, which have been suggested to strongly affect reactivity in certain reactions [22, 23]. Many investigations have been carried out using this approach, including some related to heterogeneous catalysis [21, 24].

Transition metal (TM) surfaces [25–27] and clusters [28, 29], according to recent studies, have their catalytic properties changed highly when a single atom dopant is present. Sykes and co-workers [30] demonstrated that the selectivity in catalysis provided by coinage metals (group 11) may be used in combination with other catalytically active elements that are atomically scattered. Typically, 1 % of the active dopant isolated in the host surface enables for adsorbate activation, which may be followed by overflow to the noble surface for selective catalysis [31, 32].

Computational simulations based on density functional theory can help in the design of electrocatalysts [33]. The search for efficient and stable electro-catalysts is critical since electro-catalysis is expected to be a viable clean energy conversion method. Because they identify reaction active regions and associated reaction mechanisms, theoretical simulations are critical for the rational design and performance optimization of electro-catalysts. However, there are several limits to simulating electrochemical processes under realistic conditions, such as the structures of the electrode-electrolyte interface [34].

1.3 Objectives

1.3.1 General Objectives

The main goal of this work is to develop a series of *ab initio* calculations with the Computational Hydrogen Electrode Model (CHE) [35] to understand, analyze and investigate the reduction of CO_2 as a cathodic reaction and compare its competition with HER on doped Ag(211). For this, it is necessary to study the reaction mechanism and investigate which intermediates are part of it, since the interaction between the substrate and these substances is of fundamental importance for the thermodynamic

analysis performed here.

1.3.2 Specific Objectives

- Investigate the effects of single Rh atom dopants on the adsorption properties of OH and CO on stepped Ag(211) surfaces.
- Analyze the energetic stability of the dopants at various sites on the surface.
- Compare the interactions of OH and CO molecules on doped and non doped silver surfaces.
- Examine the influence of the coordination of adsorption sites on the interaction between the molecules and the Ag(211) surface.
- Assess the impact of single-atom dopants on the catalytic activity of noble metal surfaces.
- Investigate the efficacy of single-atom silver-based alloys as electrocatalysts for CO_2 reduction.
- Evaluate the impact of surface defects on the catalytic activity of these materials.
- Analyze the interaction between host and dopant atoms in single-atom alloys, particularly concerning sharp peaks in the density of states near the Fermi energy.

Part I

Theoretical Background

2 Quantum Chemistry

2.1 Schröndiger Equation on Many Body Problem

Just as the differential equation derived from Newton's second law is the fundamental description of classical mechanics, Schröndiger's equation is equally important for describing quantum systems. It is the differential equation where the argument function is the wave function $\Psi(\mathbf{r}, t)$. The wave function, rather than being a description of the trajectory as is the response function of Newton's second law, does not itself represent a physical interpretation. Instead $|\Psi(\mathbf{r}, t)|^2$ plays a role as a probability density. The Schröndiger equation, in cases where the potential energy is not time-dependent, can be simplified to a problem in which we have a time-independent stationary wave function $\psi(\mathbf{r})$ as an argument, so we call it the time-independent Schröndiger equation, as shown in equation 2.1. $\psi(\mathbf{r})$ is called the wave function and E is the quantized energy.

$$\hat{H}\psi = E\psi. \tag{2.1}$$

$\hat{H}$ is known as the Hamiltonian, a mathematical operator that, when applied to the wave function, equals the energy times the wave function of the state associated. This Hamiltonian is the sum of all kinetic and potential energy operators of the quantum system, which can be expressed $\hat{T}$ and $V(\mathbf{r})$, respectively. There are systems in which the Schröndiger equation can be analytically solved, such as the free particle, harmonic oscillator, and others [36].

For a system with M nuclei and N electrons, the Schröndiger equation is given by equation 2.2. Where the sets $\{\mathbf{R}_i\}$ and $\{\mathbf{R}_i\}$ are position of electrons and nuclei, respectively.

$$\hat{H}(\{\mathbf{r}_i\}, \{\mathbf{R}_i\})\psi(\{\mathbf{r}_i\}, \{\mathbf{R}_i\}) = E\psi(\{\mathbf{r}_i\}, \{\mathbf{R}_i\}), \tag{2.2}$$

and the Hamiltonian is defined as:

$$\hat{H} = -\sum_{i}^{M} \frac{\hbar^2}{2M_i}\nabla^2_{\mathbf{R}_i} - \sum_{i}^{N} \frac{\hbar^2}{2m_e}\nabla^2_{\mathbf{r}_i} + \sum_{i}^{N}\sum_{j\geq i}^{N} \frac{e^2}{4\pi\epsilon_0|\mathbf{r}_i - \mathbf{r}_j|} + \sum_{i}^{M}\sum_{j\geq i}^{M} \frac{Z_i Z_j e^2}{4\pi\epsilon_0|\mathbf{R}_i - \mathbf{R}_j|} - \sum_{i}^{N}\sum_{j}^{M} \frac{Z_j e^2}{4\pi\epsilon_0|\mathbf{r}_i - \mathbf{R}_j|}. \tag{2.3}$$

Where $\hbar$ is the reduced Planck's constant, M_i is the mass of nucleus i, m_e is the mass of the electron, ϵ_0 is vacuum permittivity, e is electron fundamental charge and Z_i is the atomic number of the nucleus i. ∇^2 is the Laplacian operator. The first term in equation 2.3 is known as the nuclear kinetic energy $\hat{T}_n$, the second term is the electronic kinetic energy $\hat{T}_e$, the third and fourth terms represent the electron-electron $\hat{V}_{ee}$ and nucleus-nucleus $\hat{V}_{nn}$ Coulomb repulsion, respectively. The last term is the Coulomb attraction between an electron and a nucleus $\hat{V}_{eN}$.

If atomic units are used, the quantities $\hbar$, m_e, $4\pi\epsilon_0$ and e can be dropped since they assume unitary values. Therefore, the equation 2.3 can be simplified to 2.4.

$$\hat{H} = -\sum_{i}^{M} \frac{1}{2M_i}\nabla^2_{\mathbf{R}_i} - \sum_{i}^{N} \frac{1}{2}\nabla^2_{\mathbf{r}_i} + \sum_{i}^{N}\sum_{j\geq i}^{N} \frac{1}{|\mathbf{r}_i - \mathbf{r}_j|} + \sum_{i}^{M}\sum_{j\geq i}^{M} \frac{Z_i Z_j}{|\mathbf{R}_i - \mathbf{R}_j|} - \sum_{i}^{N}\sum_{j\geq i}^{M} \frac{Z_j}{|\mathbf{r}_i - \mathbf{R}_j|}. \tag{2.4}$$

In the rest of this chapter, all expressions will be in atomic units.

2.1.1 Born–Oppenheimer Approximation

The basic assumption in the Born-Oppenheimer approximation is that nuclei can be considered fixed, as the electron-nucleus mass ratio is very small, and thus the kinetic energy of the nuclei will be much lower than the electron´s kinetic energy. Hence, $\hat{T}_n$ can be approximated as zero. In that way, the Hamiltonian $\hat{H}$ is approximated to a total Hamiltonian $\hat{H}_{tot}$.

$$\begin{aligned} \hat{H} &= \hat{T}_e + \hat{V}_{ee} + \hat{V}_{en} + \hat{V}_{nn} \rightarrow \\ \hat{H}_{tot} &= \hat{T}_e + \hat{V}_{ee} + \hat{V}_{en} + \hat{V}_{nn} = \hat{H}_{elec} + \hat{V}_{nn}. \end{aligned} \tag{2.5}$$

It is important to note that $\hat{V}_{nn}$ is a constant for a given $\{\mathbf{R}\}$. The operator defined on V_{nn} and $\hat{H}_{elec}$ commutes. Thus, there exists a set of simultaneous eigenfunctions. The eigenvalues of H_{elec} can be determined for fixed positions of the nuclei $\{\mathbf{R}\}$. Therefore, we can define $\chi_m(\{\mathbf{r}\};\{\mathbf{R}\})$ as the eigenfunctions, which depend just parametrically on $\{\mathbf{R}\}$,

$$\hat{H}_{elec}\chi_m(\{\mathbf{r}\};\{\mathbf{R}\}) = \epsilon_m(\{\mathbf{R}\})\chi_m(\{\mathbf{r}\};\{\mathbf{R}\}), \tag{2.6}$$

and E_m as the sum between eigenvalues of the operator $\hat{H}_{elec}$ and $\hat{V}_{nm}$. We have that the eigenvalue of $\hat{H}_{tot}$ in equation 2.5 is

$$E_m\left(\{\mathbf{R}\}\right) = \epsilon_m(\{\mathbf{R}\}) + \sum_{i}^{M}\sum_{j\geq i}^{M} \frac{Z_i Z_j}{|\mathbf{R}_i - \mathbf{R}_j|}. \tag{2.7}$$

It is important to understand that $\chi_m(\{\mathbf{r}\};\{\mathbf{R}\})$ depends explicitly on electronic coordinates but only parametrically on nuclear coordinates. That means that for a different arrangement of the nuclei, there is a different configuration of $\chi_m(\{\mathbf{r}\};\{\mathbf{R}\})$. Mathematically, the complete wave function $\psi(\{\mathbf{r}\},\{\mathbf{R}\})$ (equation 2.2) can be expressed in the expansion of $\chi_m(\{\mathbf{r}\};\{\mathbf{R}\})$, having $\phi_m(\{\mathbf{R}\})$ as coefficients, depending explicitly on nuclear coordinates.

$$\psi(\{\mathbf{r}\},\{\mathbf{R}\}) = \sum_m \phi_m(\{\mathbf{R}\})\chi_m(\{\mathbf{r}\};\{\mathbf{R}\}). \tag{2.8}$$

Before we go further in the Born-Oppenheimer separation, it is important to work a bit more with $E_m(\{\mathbf{R}\})$. This quantity is related to the potential energy surface (PES). And since the PES depends only on $\{\mathbf{R}\}$, it is possible to use it to find an equilibrium configuration of the nuclei at a minimum value of $E_m(\{\mathbf{R}\})$. To make it easier to illustrate, let us consider a two-nuclei system. Suppose that the set of nuclear coordinates is $\{\mathbf{R}_1,\mathbf{R}_2\}$ and $R = |\mathbf{R}_1 - \mathbf{R}_2|$, and thus $E_m(\{\mathbf{R}\}) = E_m(R)$.

In figure 2.1, it is shown the PES curve of a diatomic system. Since R is the distance between nuclei, at minimum $E_m(R)$, we assume that this system reached the equilibrium distance R_0, and $E_m(R_0)$ is called equilibrium energy.

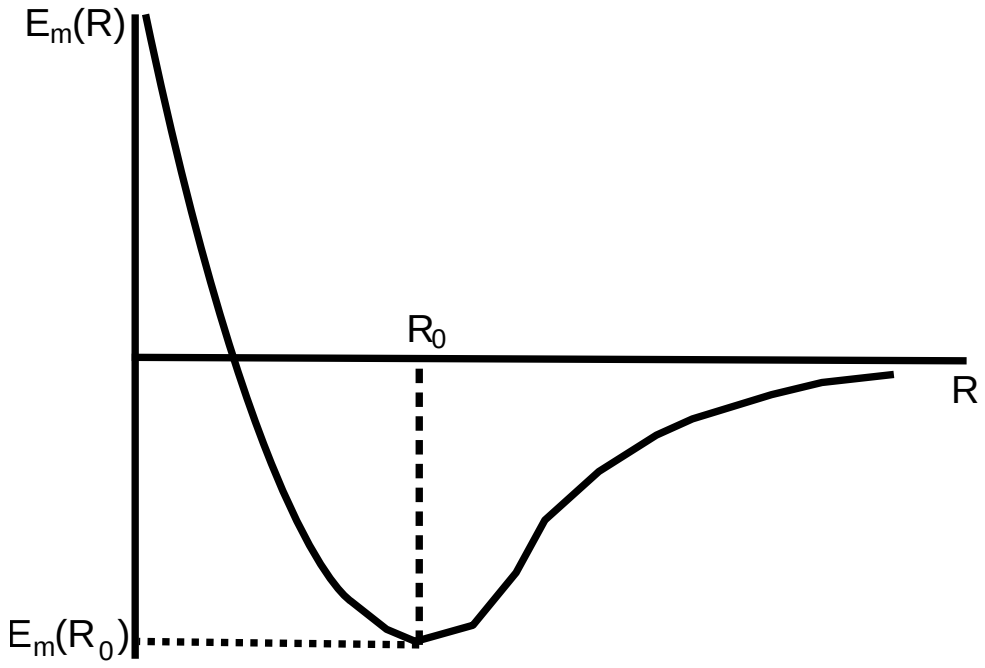


Figure 2.1: PES of diatomic system.

The Schröndiger equation, given in equation 2.2, can be written with $\hat{H}_{elec}$ on it and express the wave function by its expansion given in equation 2.8. Therefore,

$$\left(-\sum_{i}^{M}\frac{1}{2M_i}\nabla^2_{\mathbf{R}_i}+\hat{H}_{elec}+\sum_{i}^{M}\sum_{j\geq i}^{M}\frac{Z_iZ_j}{|\mathbf{R}_i-\mathbf{R}_j|}\right)\sum_{m}\phi_m(\{\mathbf{R}\})\chi_m(\{\mathbf{r}\};\{\mathbf{R}\}) = E\sum_{m}\phi_m(\{\mathbf{R}\})\chi_m(\{\mathbf{r}\};\{\mathbf{R}\}). \tag{2.9}$$

We can simplify the equation 2.9 to 2.10 by applying the electronic Hamiltonian operation $\hat{H}_{elec}$, according to equation 2.6.

$$\sum_{m}\left(-\sum_{i}^{M}\frac{1}{2M_i}\nabla^2_{\mathbf{R}_i}+\epsilon_m+\sum_{i}^{M}\sum_{j\geq i}^{M}\frac{Z_iZ_j}{|\mathbf{R}_i-\mathbf{R}_j|}\right)\phi_m(\{\mathbf{R}\})\chi_m(\{\mathbf{r}\};\{\mathbf{R}\}) = E\sum_{m}\phi_m(\{\mathbf{R}\})\chi_m(\{\mathbf{r}\};\{\mathbf{R}\}). \tag{2.10}$$

Relocating the right part to the left side of the equation 2.10 and applying the definition of E_m in the equation 2.7, we obtain equation 2.11. The operation that the first term of this equation performs on the wave function is treated mathematically separately in the equation 2.12.

$$\sum_{m}\left(-\sum_{i}^{M}\frac{1}{2M_i}\nabla^2_{\mathbf{R}_i}+E_m(\{\mathbf{R}\})-E\right)\phi_m(\{\mathbf{R}\})\chi_m(\{\mathbf{r}\};\{\mathbf{R}\})=0. \tag{2.11}$$

$$-\sum_{m}\sum_{i}^{M}\frac{1}{2M_i}\nabla^2_{\mathbf{R}_i}\left(\phi_m(\{\mathbf{R}\})\chi_m(\{\mathbf{r}\};\{\mathbf{R}\})\right) = -\sum_{m}\sum_{i}^{M}\frac{1}{2M_i}\Big[\nabla^2_{\mathbf{R}_i}\phi_m(\{\mathbf{R}\})\chi_m(\{\mathbf{r}\};\{\mathbf{R}\}) +2\nabla_{\mathbf{R}_i}\phi_m(\{\mathbf{R}\})\nabla_{\mathbf{R}_i}\chi_m(\{\mathbf{r}\};\{\mathbf{R}\})+\phi_m(\{\mathbf{R}\})\nabla^2_{\mathbf{R}_i}\chi_m(\{\mathbf{r}\};\{\mathbf{R}\}). \tag{2.12}$$

Knowing this, one may multiply equation 2.11 by $\chi^*_n(\{\mathbf{r}\};\{\mathbf{R}\})$ and integrate over all electron coordinates. This leads us to equation 2.13.

$$-\sum_{i}^{M}\nabla^2_{\mathbf{R}_i}\phi_n(\{\mathbf{R}\})-\sum_{m}\sum_{i}^{M}\frac{1}{2M_i}\int\chi^*_n(\{\mathbf{r}\};\{\mathbf{R}\})\Big\{(2\nabla_{\mathbf{R}_i}\phi_m(\{\mathbf{R}\})\nabla_{\mathbf{R}_i}\chi_m(\{\mathbf{r}\};\{\mathbf{R}\})+\phi_m(\{\mathbf{R}\})\nabla^2_{\mathbf{R}_i}\chi_m(\{\mathbf{r}\};\{\mathbf{R}\})\Big\}d^3\mathbf{r}+(E_n(\{\mathbf{R}\})-E)\phi_n(\{\mathbf{R}\})=0. \tag{2.13}$$

The terms of the equation 2.13 that still have implicit integrals can be moved to the right side of the equation. Therefore, we obtain the equation:

$$
\begin{aligned}
&-\sum_{i}^{M}\nabla^2_{\mathbf{R}_i}\phi_n(\{\mathbf{R}\})+(E_n(\{\mathbf{R}\})-E)\phi_n(\{\mathbf{R}\})= \\
&\sum_{m}\sum_{i}^{M}\frac{1}{2M_i}\Bigg\{\int 2\chi^*_n(\{\mathbf{r}\};\{\mathbf{R}\})\nabla_{\mathbf{R}_i}\chi_m(\{\mathbf{r}\};\{\mathbf{R}\})d^3\mathbf{r}\nabla_{\mathbf{R}_i}+ \\
&\qquad\int\chi^*_n(\{\mathbf{r}\};\{\mathbf{R}\})\nabla^2_{\mathbf{R}_i}\chi_m(\{\mathbf{r}\};\{\mathbf{R}\}))d^3\mathbf{r}\Bigg\}\phi_m(\{\mathbf{R}\}).
\end{aligned}
\tag{2.14}
$$

Once we got a basis set of χ_m, we may define the matrices X_{mn} and Y_{mn}. Elements on X_{nm} and Y_{nm}, with $n \neq m$ are called non-adiabatic coupling terms. If $\{\chi_m\}$ is set to be real, X is a anti-symmetric matrix. That also means that its diagonal has only elements with a value 0. Diagonal elements of Y are called non-adiabatic,

$$
X_{mn}=\int\chi^*_n(\{\mathbf{r}\};\{\mathbf{R}\})\nabla_{\mathbf{R}_i}\chi_m(\{\mathbf{r}\};\{\mathbf{R}\})d^3\mathbf{r}, \tag{2.15}
$$

$$
Y_{mn}=\frac{1}{2}\int\chi^*_n(\{\mathbf{r}\};\{\mathbf{R}\})\nabla^2_{\mathbf{R}_i}\chi_m(\{\mathbf{r}\};\{\mathbf{R}\}))d^3\mathbf{r}. \tag{2.16}
$$

With X_{mn} and Y_{mn} defined, one may define C_{nm} as the operator below.

$$
C_{nm}(\{\mathbf{R}\},\nabla_{\mathbf{R}_i})=\sum_{1}^{M}\frac{1}{M_i}\left(X_{mn}\nabla_{\mathbf{R}_i}+Y_{mn}\right). \tag{2.17}
$$

To simplify the notation, we can rewrite equation 2.14 as:

$$
\left(-\sum_{i}^{M}\nabla^2_{\mathbf{R}_i}+E_n(\{\mathbf{R}\})\right)\phi_n(\{\mathbf{R}\})=E\phi_n(\{\mathbf{R}\})+\sum_{m}C_{mn}(\{\mathbf{R}\},\nabla_{\mathbf{R}_i})\phi_m(\{\mathbf{R}\}). \tag{2.18}
$$

To continue, it was shown that at fixed nuclei positions, it can be calculated the electronic wave states and then the Born-Oppenheimer separation, in equation 2.8 can be applied, with the nuclear Hamiltonian being:

$$
\hat{H}_{Nuc}=-\left[\sum_{i}^{M}\nabla^2_{\mathbf{R}_i}+E_n(\{\mathbf{R}\})+\sum_{n}C_{mn}(\{\mathbf{R}\},\nabla_{\mathbf{R}_i})\right]. \tag{2.19}
$$

So, the effective potential that the nuclei experience is $E_n(\{\mathbf{R}\}+\sum_n C_{mn}(\{\mathbf{R}\},\nabla_{\mathbf{R}_i})$. In the equation below, it is considered the nuclear Hamiltonian $\hat{H}_{Nuc}$ with the adiabatic approximation, in which all terms of matrices in $C_{mn}(\{\mathbf{R}\}$ are zero. Then, the effective potential is the PES and the eigenvalue of $\hat{H}_{Nuc}\phi_n(\{\mathbf{R}\})$ is the total energy of the system.

$$
\hat{H}_{Nuc}=-\sum_{i}^{M}\nabla^2_{\mathbf{R}_i}+E_n(\{\mathbf{R}\})=\hat{T}_n+E_n(\{\mathbf{R}\}), \tag{2.20}
$$

$$
\hat{H}_{Nuc}\phi_n(\{\mathbf{R}\})=E_n\phi_n(\{\mathbf{R}\}). \tag{2.21}
$$

Hence, the Born-Oppenheimer approximation is actually the imposition of equation 2.8 and the use of the PES as the effective potential for the nuclear movement. We can solve the Schrödinger equation by separating the problem in an electronic equation 2.6 and a nuclear equation 2.21.

2.2 Density Functional Theory

2.2.1 Introduction

We know that finding the exact solution for the equations like 2.6 is very complicated and often impossible. Given this, it is clear that approximations are needed for practical implementation to be feasible. The definition of electron density is extremely important to describe quantum systems. The probabilistic interpretation that the square of the wave function has, directly gives the core definition of the electron density $\rho(\mathbf{r})$. Mathematically, we should understand this function as a probability density (thus, non-negative) that determines the probability of finding one electron inside an element of volume $d\mathbf{r}_1$ with an arbitrary discrete spin value s_1, assuming that there are $N-1$ electrons in arbitrary position and spin. The equation 2.22 shows the expression that defines it by integrating over spin coordinates of all electrons and over spatial coordinates $\{\mathbf{r}\}$. The notation $\mathbf{x}_i$ is the set of $(\mathbf{r}_i, \mathbf{s}_i)$.

$$\rho(\mathbf{r}) = N \int \cdots \int |\psi(\mathbf{x}_1, \mathbf{x}_2, \ldots, \mathbf{x}_N)|^2 ds_1 d\mathbf{x}_2 \ldots d\mathbf{x}_N. \tag{2.22}$$

The particles are indistinguishable, so the probability of finding any electron at a position within the volume element is simply N times the probability of finding a particular electron. Also, as shown in equation 2.23 and 2.24, the electron density needs to integrate into the total number of electrons and vanish at infinity, respectively.

$$\int \rho(\mathbf{r}) d\mathbf{r}_1 = N. \tag{2.23}$$

$$\lim_{|r|\to\infty} \rho(\mathbf{r}) = 0. \tag{2.24}$$

Observing these properties, we have that in the position where a nucleus is located, $\rho(\mathbf{r})$ delivers a local finite maximum and its gradient delivers a discontinuity, characterizing this point as a cusp. The equation 2.25 shows that the cusp property is strongly related to the nuclear charge Z_A. The part of the Hamiltonian $-\frac{Z_A}{r_{iA}}$ demonstrates the singularity when the electron-nucleus distance is close to zero.

$$\lim_{r_{iA}\to 0} \left[\frac{\delta}{\delta \mathbf{r}} + 2Z_A \right] \rho(\mathbf{r}) = 0. \tag{2.25}$$

Before describing the importance of $\rho(\mathbf{r})$ for computational chemistry, experimentally this function is observed and measurable (using X-ray diffraction, for example), unlike $\psi(\mathbf{x}_1, \ldots, \mathbf{x}_N)$. Furthermore, the wave function, or even a good approximation of it, is

very complicated to deal with, since it is dependent on $4N$ variables (3 spatial and 1 spin for each particle), even delivering all the information of a quantum system. Therefore, the computational manipulation of systems, studied in chemistry and materials science, which contain many particles becomes not only very difficult but often impossible. The electron density $\rho(\mathbf{r})$ is a quantity that depends only on three spatial variables and therefore is an object of study, with which a well-understood method can try to reach a satisfactory solution for the Schröndiger equation [37].

2.2.2 Hohenberg-Kohn Theorems

First Hohenberg-Kohn Theorem

The first theorem necessary for the development of density functional theory (DFT) was presented in a 1964 paper by Hohenberg and Kohn. The direct quote is "*the external potential $v(\mathbf{r}_i)$ is a unique functional of $\rho(\mathbf{r})$; since, in turn, $v(\mathbf{r}_i)$ fixes $\hat{H}$, we see that the full many-particle ground state is a unique functional of $\rho(\mathbf{r})$*" [38]. The potential $v(\mathbf{r})$ is the expectation value of the operator $\hat{V}_{eN}$ (presented in equation 2.5). In other words, if we consider that $v(\mathbf{r}_i)$ fixes a Hamiltonian, there's a unique ρ for this. We are going to show this by a logical statement called *Reductio ad absurdum* (reduction to absurdity).

The deny statement is to consider that we got two different external potentials $v(\mathbf{r}_i)$ and $v'(\mathbf{r}_i)$. Therefore, there would have two fixed Hamiltoniansassociated $\hat{H}$ and $\hat{H}'$, respectively. And also, there would have two wave functions of ground-state as the solution of the Schröndiger Equation Ψ and Ψ'. To summarize, see the equations below.

$$v \Rightarrow \hat{H} \Rightarrow \Psi \tag{2.26}$$

and

$$v' \Rightarrow \hat{H}' \Rightarrow \Psi'. \tag{2.27}$$

As we are talking about two distinct functions, $E_0 \neq E_0'$. However, to make it possible we need to assume that both wave functions yield a unique ground state $\rho(\mathbf{r})$. This is really possible since we are dealing with the square of wave functions. So,

$$v \Rightarrow \hat{H} \Rightarrow \Psi \Rightarrow \rho(\mathbf{r}) \Leftarrow \Psi' \Leftarrow \hat{H}' \Leftarrow v', \tag{2.28}$$

note that Ψ' is an exact ground state of Schrodinger equation solution for the $\hat{H}'$ problem. However, it is a trial function for $\hat{H}$. The same can be observed to Ψ to $\hat{H}$ and $\hat{H}'$. Using the variational principle (no trial wave function can generate an expected value lesser than the ground state delivered by the exact wave function) we can observe 2.29 and 2.30:

$$E_0 < \langle \Psi' | \hat{H} | \Psi' \rangle \,, \tag{2.29}$$

analogously,

$$E_0' < \langle \Psi | \hat{H}' | \Psi \rangle \,. \tag{2.30}$$

We can manipulate both equations to compare the inequality and the increments by the difference of both hamiltonians $\hat{H}$ and $\hat{H}'$, $\langle\Psi'|\hat{H}'|\Psi'\rangle$. Like shown in equation 2.31.

$$E_0 < \langle\Psi'|\hat{H}|\Psi'\rangle = \langle\Psi'|\hat{H}'|\Psi'\rangle + \langle\Psi'|\hat{H} - \hat{H}'|\Psi'\rangle\,. \tag{2.31}$$

That means that the variational integral is $\langle\Psi'|\hat{H}'|\Psi'\rangle$ increments by the difference of both hamiltonians $\hat{H}$ and $\hat{H}'$. The potential energy v changes does not imply the change of electron kinetic energy $\hat{T}$ and $\hat{V}_{ee}$. That way,

$$E_0 < \langle\Psi'|\hat{H}|\Psi'\rangle = \langle\Psi'|\hat{H}'|\Psi'\rangle + \langle\Psi'|\hat{T} + \hat{V}_{ee} + v - \hat{T} - |\Psi'\rangle\,. \tag{2.32}$$

Taking the expression given in the equation 2.32, the kinetic energy operators of the electrons and the interaction between the electrons are equal parts that $\hat{H}$ and $\hat{H}'$ share. So, the equation 2.33 shows the same expression with canceled terms.

$$E_0 < \langle\Psi'|\hat{H}|\Psi'\rangle = \langle\Psi'|\hat{H}'|\Psi'\rangle + \langle\Psi'|v - v'|\Psi'\rangle\,. \tag{2.33}$$

The expression of applied v is known as

$$\langle\Psi|v|\Psi\rangle = \int \rho(\mathbf{r})v d\mathbf{r}, \tag{2.34}$$

the first term on the right side of equation 2.33 is simply the ground state E_0'. Therefore, we can substitute such terms of the equation for 2.35.

$$E_0 < E_0' + \int \rho(\mathbf{r})\{v - v'\}d\mathbf{r}. \tag{2.35}$$

If we obtain the equation 2.35, we have the expression

$$E_0' < E_0 + \int \rho(\mathbf{r})\{v' - v\}d\mathbf{r} \tag{2.36}$$

and if equations 2.35 and 2.36 are combined, one gets

$$E_0' + E_0 < E_0 + E_0'. \tag{2.37}$$

which is a contradiction. And that is why we cannot consider the affirmation. That proves the existence of a unique ground-state density. ρ_0 is the ground state density. Using this terminology and the functional expressions, we get equation 2.38.

$$E[\rho_0] = T[\rho_0] + V_{ee}[\rho_0] + V_{en}[\rho_0]. \tag{2.38}$$

The equation 2.38 shows the functional expressed by $V_{eN}[\rho_0]$. Since nuclei are fixed due to the Born-Oppenheimer approximation consideration, equation 2.38 turns to equation 2.39.

$$E[\rho_0] = T[\rho_0] + V_{ee}[\rho_0] + \int \rho_0(\mathbf{r})V_{eN}d\mathbf{r}. \tag{2.39}$$

The first two terms of equation 2.39 form a functional called Hohenberg-Kohn functional $F_{HK}[\rho_0]$. That way equation 2.39 turns to:

$$E[\rho_0] = F_{HK}[\rho_0] + \int \rho_0(\mathbf{r}) V_{eN} d\mathbf{r}. \tag{2.40}$$

The functional $F_{HK}[\rho_0]$ is a sum of kinetic energy and electron-electron repulsion operator. That is an interesting functional once it is completely independent of the system we are trying to solve. For instance, it can be applied to a hydrogen atom or in DNA molecules, and still, that is going working equally. Nevertheless, T and V_{ee} do have not a known explicit form. We are completely in dark about those two functionals.

Second Hohenberg-Kohn Theorem

This is known as the variational principle of Hohenberg-Kohn. The important thing now is that we know that the density gives us all the properties of the ground state. The trial density $\tilde{\rho}$ is a useful tool for this theorem. In a rough way, this theorem states that F_{HK} delivers the lowest energy if and only if the input density is the true ground state density ρ_0. Now, let's apply this trial to the Energy functional:

$$E_0 \leq T[\tilde{\rho}] + V_{ee}[\tilde{\rho}] + E_{Ne}[\tilde{\rho}]. \tag{2.41}$$

The density $\tilde{\rho}$ has to be N-representable. it is important to remember that any trial density yields its own Hamiltonian $\hat{H}$ and hence its own wave function $\tilde{\Psi}$. From the variational principle, we consider this:

$$\langle \Psi | \hat{H} | \Psi \rangle = T[\tilde{\rho}] + V_{ee}[\tilde{\rho}] + E_{Ne}[\tilde{\rho}] = E[\tilde{\rho}] \geq E_0[\rho_0] = \langle \Psi_0 | \hat{H} | \Psi_0 \rangle , \tag{2.42}$$

just as desired.

2.2.3 Kohn-Sham Equations

Kohn-Sham equations are fundamental for practical implementations of DFT. it is an interesting concept as it attacks the many body problem with a perspective of fictional non-interacting electrons and provides a practical way to develop accurate approximate functionals.

Reminding ourselves of the Hohenberg-Kohn definition, we have a definition for many body systems provided by the functionals of electron density. That is given by the universal functional $F[\rho]$ and the functional of external potential given by the integral bellow

$$E[\rho] = \int \rho(\mathbf{r}) v(\mathbf{r}) d\mathbf{r} + F[\rho(\mathbf{r})], \tag{2.43}$$

and this universal functional can be expressed by

$$F[\rho] = T[\rho(\mathbf{r})] + J[\rho(\mathbf{r})] + E_{ncl}[\rho(\mathbf{r})]. \tag{2.44}$$

Where $T[\rho(\mathbf{r})]$ is the kinetic energy functional, $J[\rho(\mathbf{r})]$ is the classical Coulomb interaction and E_{ncl} is a non-classical portion. J and $E_{ncl}[\rho(\mathbf{r})]$ sum up to V_{ee}. There, only $J[\rho(\mathbf{r})]$ has an explicit known dependence on the density $\rho(\mathbf{r})$. While the unknown kinetic energy has a large impact, and cannot be neglected.

Thomas and Fermi tried to come up with a simple functional that may explicit the kinetic energy $T[\rho(\mathbf{r})]$.

$$\int \rho^{5/3}(\mathbf{r})d\mathbf{r}. \tag{2.45}$$

However, such a simple model-dependent approach led to disappointing results. Kohn-Sham Equation attacks the $T[\rho(\mathbf{r})]$ problem in a different way. Assuming a fictitious non-interacting reference system, a Hamiltonian $\hat{H}_S$ that contains an effective local potential $V_s(\mathbf{r})$ is written as:

$$\hat{H}_S = -\frac{1}{2}\sum_i^N \nabla_i^2 + \sum_i^N V_s(\mathbf{r}). \tag{2.46}$$

So this operator does not contain any interaction between electrons, thus it describes in fact a non-interacting system. Therefore, equation 2.47 provides wave function of N electrons that do not interact with each other while also obeying the antisymmetry principle. Consequently, its ground state wave function is expressed through a Slater determinant (emphasizing that these new quantities are distinct from those in the Hartree-Fock model).

$$\Phi_s = \frac{1}{\sqrt{N!}}\begin{vmatrix} \phi_1(\mathbf{r}_1) & \phi_2(\mathbf{r}_1) & \cdots & \phi_N(\mathbf{r}_1) \\ \phi_1(\mathbf{r}_2) & \phi_2(\mathbf{r}_2) & \cdots & \phi_N(\mathbf{r}_2) \\ \vdots & \vdots & \ddots & \vdots \\ \phi_1(\mathbf{r}_N) & \phi_2(\mathbf{r}_N) & \cdots & \phi_N(\mathbf{r}_N) \end{vmatrix}, \tag{2.47}$$

Φ is a Slater determinant, and ϕ_i are spin-orbitals, which are determined by the equation:

$$\hat{f}^{KS}\phi_i = \epsilon_i\phi_i. \tag{2.48}$$

The one-electron Kohn-Sham operator $\hat{f}^{KS}$ is defined as:

$$\hat{f}^{KS} = -\frac{1}{2}\nabla_i^2 + V_s(\mathbf{r}). \tag{2.49}$$

What matters, after basing this artificial system, is to establish the potential V_S so that the sum of the squared modulus of the orbitals $\{\phi_i\}$ is exactly the ground state density of the real interacting problem.

$$\rho_S(\mathbf{r}) = \sum_i^N \sum_s |\phi_i(\mathbf{r}, s)|^2 = \rho_0(\mathbf{r}). \tag{2.50}$$

Finding the best determination of kinetic energy is still a problem that has to be addressed. The idea is to know that if it is not possible to accurately determine the kinetic energy through an explicit a functional, one should conceptualize an approximate functional that delivers a satisfactory answer being computationally possible to be implemented. Taking the non-interacting system, the kinetic energy T_S is given by the equation,

$$T_S = \sum_i^N \langle \phi_i | -\frac{1}{2}\nabla^2 | \phi_i \rangle . \tag{2.51}$$

Logically, $T_S \neq T$. However, they share the same density. Accounting for that, the functional below is introduced.

$$F[\rho(\mathbf{r})] = T_s[\rho(\mathbf{r})] + J[\rho(\mathbf{r})] + E_{XC}[\rho(\mathbf{r})], \tag{2.52}$$

where E_{XC} is the exchange-correlation energy and its definition takes account of the residual part of the true kinetic energy (T_C).

$$E_{XC}[\rho(\mathbf{r})] = (T[\rho(\mathbf{r}])] - T_s[\rho(\mathbf{r}])]) + (V_{ee}[\rho(\mathbf{r}])] - J[\rho(\mathbf{r}])]) = T_c[\rho(\mathbf{r})] + E_{ncl}[\rho(\mathbf{r})]. \tag{2.53}$$

Basically this energy deals with everything that differs from the fictitious system. it is important to mention that if E_{XC} was known, which is not the case, the Kohn-Sham procedure would lead to the exact energy. The formalism here expressed is not an approximation, the KS equation is in principle exact. However, the principal goal now is to find E_{XC} that we do not have. Actually, this is the central part of it [37].

2.2.4 Exchange–Correlation Functionals

The differentiation among the various applications of the DFT method is related to the choice of the exchange-correlation functional. As mentioned in the previous section, the energy functional must be free from self-interaction, implying that the exchange energy for a one-electron system, such as the hydrogen atom, should exactly cancel out the Coulomb energy, while the correlation energy should be zero [39]. Exchange-correlation functionals are defined by a mathematical form that, like other empirical methods, includes parameters. There are two main approaches to determine these parameters. The first one is based on requiring the functional to meet certain criteria, such as

- When the density becomes constant, the result of the uniform electron gas should be recovered. While this is a valid and important mathematical requirement for applications in solid-state physics, it may not be as relevant for chemical applications, given that molecular densities are relatively poorly described by uniform electron gas methods.
- The coordinated scaling of the exchange energy should be linear, meaning that multiplying the electron coordinates by a constant factor should result in a similar linear scaling of the exchange energy.
- There is no direct scaling law for correlation energy, but scaling the electron coordinates by a factor greater than 1 should increase the magnitude of correlation (and vice versa). At low densities, scaling becomes linear, similar to exchange energy.

- As the scaling parameter tends to infinity, the correlation energy for a finite system approaches a negative constant [39].

Another approach involves fitting available parameters to experimental data. A combination of these approaches is often used in practice. The quality of exchange-correlation functionals ultimately needs to be assessed by comparing their performance with experiments or high-level quantum mechanical calculations.

The Local Density Approximation (LDA) assumes that the density can be treated as a locally uniform gas of electrons or as a slowly varying function. The exchange energy for a uniform electron gas follows Dirac's formula. In more general cases, where the densities of the spin components are not equal, the LDA (where the sum of densities is raised to the power of 4/3) has been largely replaced by the Local Spin Density Approximation (LSDA), where individual densities are raised to the power of 4/3.

The Generalized Gradient Approximation (GGA) extends beyond the LDA by including information about the gradient of the electronic density. GGA methods are referred to as "semi-local", although they depend only on the density and its derivatives at a specific point. The inclusion of density gradient allows for a better description of systems with strong chemical bond and magnetic properties. GGA functionals are widely used in electronic structure calculations of molecules and materials due to their ability to more accurately capture the effects of electronic correlation in complex systems. J. P. Perdew and coworkers [40] have proposed an exchange-correlation functional aimed at eliminating spurious oscillations in the first-order Taylor-like expansion and ensuring that the exchange and correlation holes integrate to the required values of 1 and 0. This functional (PBE) is the one employed in this work.

2.3 Computational Hydrogen Electrode Model

To model the selected steps of CO_2RR using the proton-coupled electron transfer (PCET) approximation, we employed the computational hydrogen electrode (CHE) model [41, 42]. This model enables the incorporation of applied potentials (U) to a reference hydrogen electrode (RHE) operating under reversible conditions. At zero potential ($U = 0\,\mathrm{V}$ vs. RHE) and under any pH and temperature, the reaction

$$\frac{1}{2}\mathrm{H_2} \rightleftharpoons \mathrm{H^+} + e^- \ , \tag{2.54}$$

is considered to be at equilibrium. The applied potential can be included in the free energy as $G_{\mathrm{H^+}+e^-} = 0.5 \cdot G_{\mathrm{H_2}} - eU$, where eU is the energy applied by a potential U [41, 42]. The onset potential (U_{onset}) is the potential value at which the necessary energy is applied for the reaction to overcome its rate-limiting step and in this model can be obtained from the reaction step with the largest free energy increase (ΔG_{max}) as $U_{onset} = -\Delta G_{max}/e$.

The total Gibbs free energy for each reaction step is calculated using the following equation,

$$\Delta G = \Delta E_{tot} + \Delta E_{sol} + ZPE + \int C_p dT - TS \ , \tag{2.55}$$

where E_{tot} is the total energy calculated by the DFT geometry optimization and ΔE_{sol} is the solvation energy correction proposed by Rendón-Calle et al [43]. From the vibrational frequencies calculated for the adsorbed molecules, we extract the ZPE (zero-point energy), $\int C_p dT$ and $-TS$ (enthalpic and entropic correction) terms. These terms were computed at 298,15 K under the harmonic limit using the thermochemistry module of the atomic simulation environment package [44] as:

$$ZPE = \sum_i \frac{1}{2}\epsilon_i, \tag{2.56}$$

$$\int C_p dT = \sum_i \frac{\epsilon_i}{e^{\frac{\epsilon_i}{k_B T}} - 1}, \tag{2.57}$$

$$S = k_B \sum_i \frac{\epsilon_i}{k_B T(e^{\frac{\epsilon_i}{k_B T}} - 1)} - \ln\left(1 - e^{\frac{\epsilon_i}{k_B T}}\right), \tag{2.58}$$

where ϵ_i are the energies of the vibrational modes, k_B is the Boltzmann constant, and T is the temperature.

2.4 CO_2 Reduction Reaction

We evaluate the suitability of each SAAC as an active site for CO_2RR to products more reduced than CO using four criteria based on literature information:[12, 45] (*i*) The CO adsorption must be strong enough to prevent CO desorption; (*ii*) the difference $G_{CHO} - G_{CO}$ or $G_{COH} - G_{CO}$ must be small enough to permit the first reduction of *CO; (*iii*) the OH adsorption should be weak enough to avoid the site being poisoned by *OH; (*iv*) the HER predicted based on H adsorption should not dominate the reaction on this site.

Figure 2.2 illustrates all the stages of PCETs involved in the possible pathways of CO_2 reduction. Each step consists of several intermediates that can either remain adsorbed and continue in the reaction or desorb and terminate the reaction.

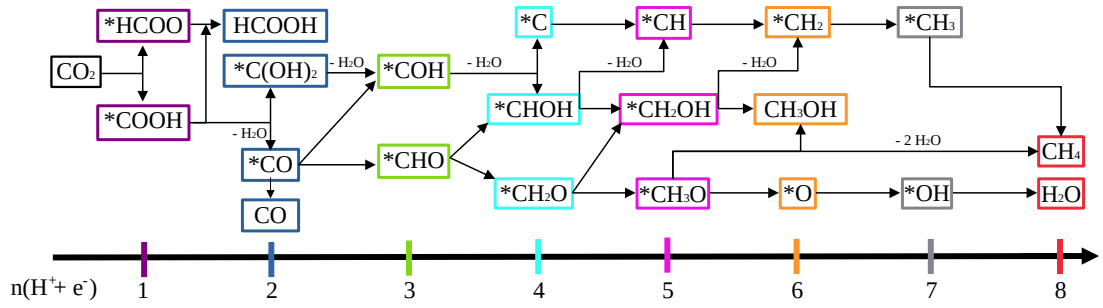


Figure 2.2: Complite possible reaction pathways for reducing CO_2 to CO, HCOOH, CH_3OH, and CH_4 involve a sequence of PCET.

Figure 2.3 offers a simplified depiction of the CO_2RR pathways toward CO, CH_4, and methanol (CH_3OH), alongside the competing HER step and the surface hydrogenation

of OH. As discussed earlier, undoped Ag is effective in generating CO due to its low adsorption energy. Based on the assumption from Cheng et al. (2016), we anticipate that the conversion of CO_2 to CO will predominantly occur near the Ag atoms, with CO being primarily bound to the single-atom dopant, facilitating subsequent steps. Figure 2.3 delineates (using dashed arrows) the specific steps we investigate in this study to identify a single-atom catalyst that meets the outlined criteria.

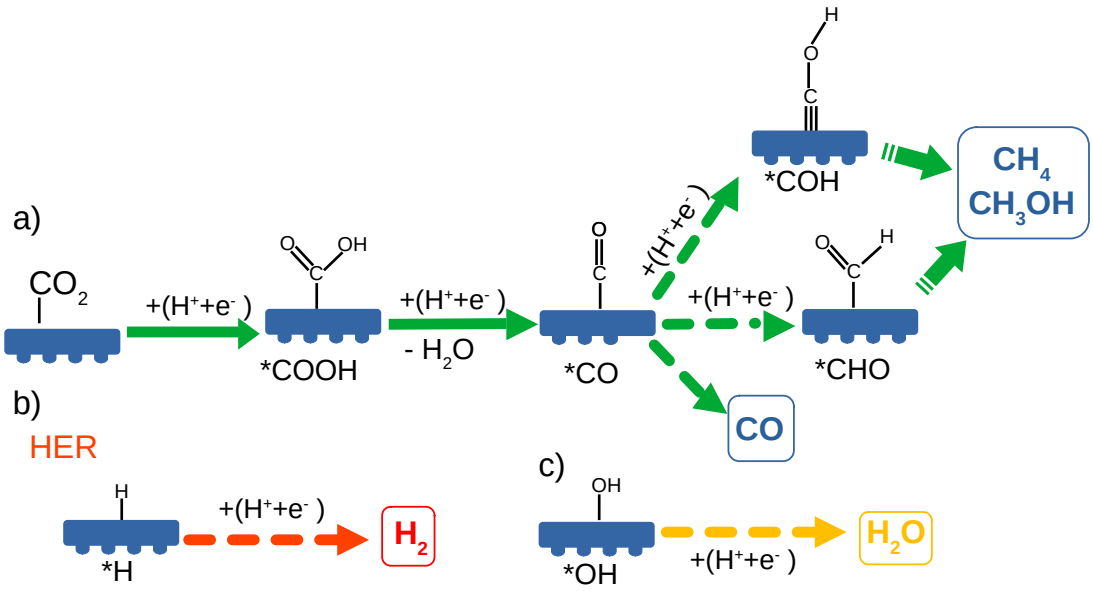


Figure 2.3: Steps CO_2RR and HER given by pathway green and red, respectively. The blue platform represents the substrate Ag(211). Reproduced from [1], with the permission of AIP Publishing.

Experimentally and computationally, Ag has been shown to present high efficiency to form CO, and therefore, this work aims to analyze if any dopant favors the formation of COH or CHO to the detriment of CO desorption [18, 46, 47].

3 Computational Details

3.1 Computational Methodology

We have performed all DFT calculations using the Vienna *ab initio* simulation package (VASP),[48–50] version 5.4.4. For the exchange-correlation (XC) energy functional, the semilocal Perdew—Burke—Ernzerhof (PBE) formulation [51] was used in addition to the projector augmented-wave (PAW) method,[50, 52]. DFT-PBE has been shown to have problems in describing long-range van der Waals interactions in weakly interacting molecular systems [53–55]. We used the semi-empirical pairwise D3 correction with zero-damping function [53], to improve the description of such interactions, which adds an energy contribution to the DFT-PBE total energy. The D3 adjustment has been used successfully in a number of surface science research [21, 56–58].

Table 3.1 shows the PAW-PBE projectors. Also, for all species, the number of valence electrons (`ZVAL`) and the recommended plane-wave cutoff energy by the projector (`ENMAX`) are given.

Table 3.1: Relevant parameters of the PAW projectors. For each element, we show the chosen projector, the number of valence electrons (`ZVAL`), the electronic configuration, and the recommended plane-wave cutoff energy (`ENMAX`).

Element	PAW-PBE Projectors	`ENMAX` (eV)	Eletronic Configuration	`ZVAL`
Ag	Ag_GW 06Mar2008	249.844	[Kr] $4d^{10}5s^1$	11
C	C_GWnew 19Mar2012	413.992	[He] $2s^22p^2$	4
O	O_GWnew 19Mar2012	434.431	[He] $2s^22p^4$	6
H	H_GW 21Apr2008	300.000	$1s^1$	1
Co	Co_GW 31Mar2010	323.400	[Ar] $3d^7\ 4s^2$	9
Cu	Cu_GW 19May2006	417.039	[Ar] $3d^{10}4s^1$	11
Fe	Fe_GW 31Mar2010	321.007	[Ar] $3d^64s^2$	8
Ni	Ni_GW 31Mar2010	357.323	[Ar] $3d^84s^2$	10
Ir	Ir_sv_GW 23Mar2010	319.843	[Xe] $4f^{14}5d^76s^2$	17
Rh	Rh_GW 06Mar2008	247.408	[Kr] $4d^85s^1$	9

For the Brillouin zone (BZ) integration, we used a Monkhorst—Pack **k**-mesh of $17 \times 17 \times 17$ on bulk Ag in the face-centered cubic (fcc) structure calculation. This higher grid was used to determine Ag lattice parameters. For that stress tensor calculation, it was used plane-wave cutoff energy of 499,77 eV. The Ag(211) surface geometry (and its dopant variant) was modeled as repeated slab with 15 layers, 3×1 surface unit cell, vacuum thickness of 16 Å, and lattice constant of 4,07 Å. It was used a **k**-mesh of 4×5×1 with a plane-wave cutoff energy of 488,725 eV (12,5 % larger the recommended among all species considered in this thesis H, C, O, Co, Cu, Fe, Ni, Ir, Rh, and Ag).

Gas-phase molecules and free-atoms were calculated using the Γ-point for the Brillouin zone integration, with 488,735 eV for the plane-wave cutoff energy. The molecule/atom was placed in the center of a large unit cell with $15 \times 15.25 \times 15.50$ Å. A non-cubic format was considered to ensure that all distances between molecules and their repetitions were not less than 15 Å.

3.2 Adsorption on Stepped Surfaces

The present work is focused on the computational description of how differently coordinated sites on the Ag(211) surface affects its interaction with the molecules (CO, OH, COH, CHO, and H). The effect of a single atom dopant on this noble metal stepped surface is also studied, being TM dopant selected due to its known catalytic activity[59, 60]. The main goal is therefore to provide a deeper atomistic understanding of the interactions between the doped and non-doped surfaces with molecular species involved in electrocatalysis, together with highlighting the effect of defects on such surfaces.

The stepped Ag(211) surface is composed by an open one-atom (100) step and a compact 3-atom wide (111) terrace,[61, 62] as indicated in Figure 3.1. In the ideal Ag(211) surface, the Ag atoms exposed to the vacuum region have different coordination

environments. To characterize the coordination of the atoms exposed to the vacuum region, we employed the effective coordination concept,[63, 64] which is described in more detail in the next section. The results are shown in color codes in Figure 3.1-c, which will be used to improve our understanding on the role of adsorption site coordination in the adsorption properties [65, 66].

For the substitutional doping in the topmost Ag(211) surface layer, a single Ag atom exposed to the vacuum region was replaced by TM dopant either on a step, terrace, or at the corner position, as indicated in Figure 3.1-b, generating the systems named as step-TM@Ag(211), terrace-TM@Ag(211), and corner-TM@Ag(211), respectively. Therefore, subsurface doping was not considered in this study.

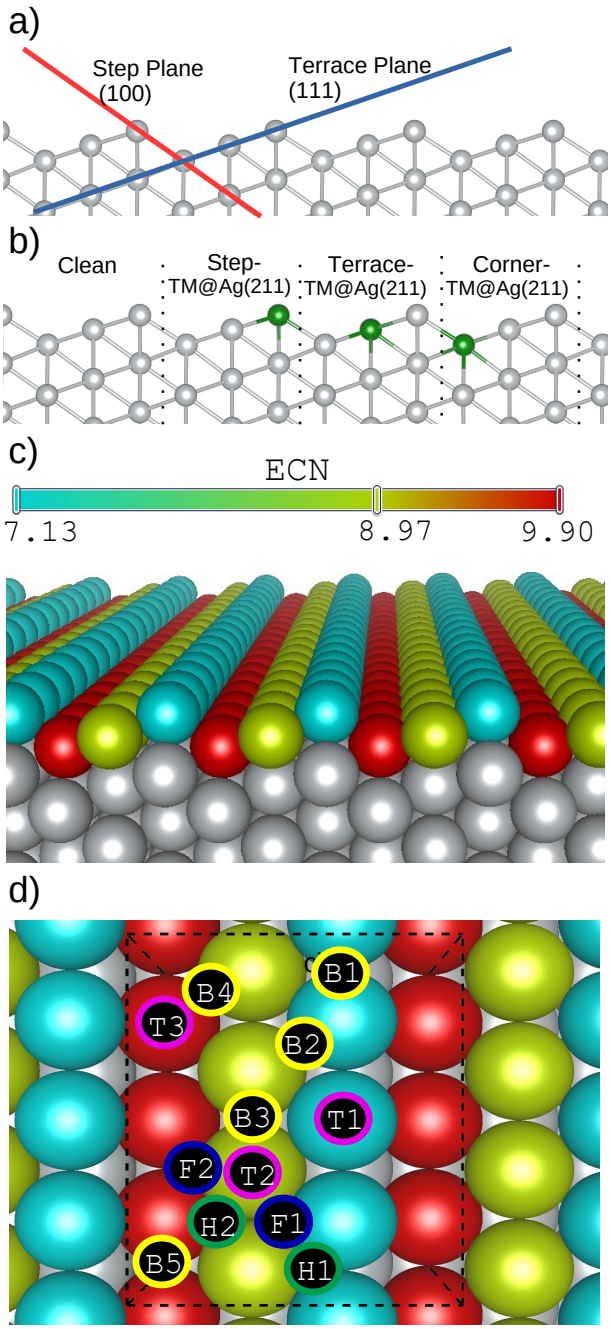


Figure 3.1: Representation of the Ag(211) surface: a) Illustration showing the intersection of step and terrace planes. b) Identification of potential dopant positions. c) Side view and d) top view of the Ag(211) surface, with atoms exposed to the vacuum colored based on their effective coordination number values. Adsorption sites are categorized into several groups: top (T1, T2, and T3), bridge (B1, B2, B3, B4, and B5), hollow hcp (H1, H2), and hollow fcc (F1, F2) sites. These two last forms differ from each other in their packing factor. Reproduced from Ref. [2] with permission from the Royal Society of Chemistry.

For the adsorption of molecules on clean and TM-doped Ag(211) surfaces, we selected the high-symmetry adsorption sites for the initial location of the diatomic molecules, which were separated into four groups. For example, three top (T1, T2, and T3), five bridge (B1, B2, B3, B4, and B5), two hollow hcp sites (H1 and H2) and two hollow fcc sites (F1 and F2), Figure 3.1-d. CO was initially set up with the C atom pointing towards the surface, while OH binds via the oxygen atom. For the COH and CHO molecules, the initial structure was arranged so that the carbon was the atom closest to the substrate. For all cases, we considered the adsorbate only on one side of the slab, while two Ag layers at the bottom of the slab were frozen in their relaxed clean surface positions and the remaining atoms were relaxed along the geometry optimization without symmetry constraints.

3.3 Geometric Parameters

3.3.1 Effective Coordination Number

Coordination numbers (CN) are useful concepts for rationalizing the properties of different surfaces. This quantity is expressed simply as the number of nearest neighbors of a given i atom and is assumed to have an integer value. This concept can be improved by assigning different weights to each neighbor, depending on the distance between atoms (d_{ij}). In this work, we use the concept of effective coordination numbers (ECNs) [63, 64]. CN is said to be defined as unit weight. We may use the weight function $w_{ij} \neq 1$ to learn more about the environment and calculate the bond length between i and j. Chemically, including all i-j bond strengths in the model contributes significantly to the system´s description. To begin, we define the average bond length of atom i as

$$d_{av}^{i} = \frac{\sum_j d_{ij} \exp\left[1 - \left(\frac{d_{ij}}{d_{av}^{i}}\right)^6\right]}{\sum_j \exp\left[1 - \left(\frac{d_{ij}}{d_{av}^{i}}\right)^6\right]}, \tag{3.1}$$

which is calculated self-consistently numerical method. Atom i's effective coordination number (ECN^i) is

$$\mathrm{ECN}^i = \sum_j \exp\left[1 - \left(\frac{d_{ij}}{d_{av}^{i}}\right)^6\right]. \tag{3.2}$$

Equations 3.1 and 3.2 are components of a technique in which exponential functions and powers of 6 are used as weighting functions. The exponential term leads to diminishing weights of the distances as the length increases [67]. Since its introduction, it has become available for many Bravais lattices Structure. The use of specific functions, such as the sixth power, in determining ECN in crystalline structures is based on crystal structure theory and the geometry of atomic arrangements [63, 64, 67].

We computed the shortest distances between the molecule and the surface (O-TM and C-TM lengths) and the ECN of the molecule´s closest atom to the surface to define the geometric parameters of the adsorption system. [63, 64] In each calculation, the

surface-to-probe distance also aided in characterizing the molecule's final adsorption location. By comparing different adsorption sites, we can better understand the influence of coordination on adsorption energies. Values of ECN are also defined for some atoms belonging to the doped or clean surface, the dopant, and the corresponding silver atom.

3.4 Energetic Parameters

The binding energies (E_b) of molecular species employed as probes (CO, OH) are computed using the following equations:

$$E_b = E_{tot}^{mol} - \sum E_{tot}^{i} \ , \tag{3.3}$$

where E_{tot}^{mol} is the total energy of the molecules in gas-phase and E_{tot}^{i} is the total energy of the free atoms. To characterize the interaction of molecules with surfaces, we determined the adsorption energy (E_{ad}), which is given by the equation below.

$$E_{ad} = E_{tot}^{mol/sub} - E_{tot}^{sub} - E_{tot}^{mol} \ , \tag{3.4}$$

where $E_{tot}^{mol/sub}$ denotes the total energy for the adsorbed configuration, and E_{tot}^{sub} and E_{tot}^{mol} denote the total energies of the substrate and molecule, respectively.

3.5 Electronic Parameters

Work function (φ) is defined as the minimum energy required to extract one electron from a metal. It is one of the fundamental electronic properties of bare and coated metallic surfaces [68]. The slab's φ is computed using the equation $\varphi = V_{elec}(\mathbf{r}_{vac}) - \epsilon_{\text{Fermi}}$, where $V_{elec}(\mathbf{r}_{vac})$ is the electrostatic potential in the vacuum area far from the surface and ϵ_{Fermi} is the Fermi energy. The effective Bader charge of a species i, Q_{eff}^{i}, is defined over an analysis that represents a computational chemistry technique used to dissect the charge density of a system into distinct regions associated with individual atoms. At its core, the Bader charge of an atom is defined within a designated volume called a Bader volume, determined by tracing the gradient flow of the charge density. Bader charge integration entails pinpointing the attraction basins of fixed points within the charge density distribution. These fixed points correspond to local maxima of the charge density, acting as the core centers of the Bader volumes [69]. it is computed as $Q_{eff}^{i} = Q_{\text{Bader}}^{i} - Z_{val}$, where Z_{val} represents the atom's valence and Q_{Bader}^{i} represents the Bader charge [70]. The electronic density difference ($\Delta\rho(\mathbf{r})$) is derived by subtracting the density of the adsorbed system ($\rho^{mol/sub}$), isolated molecule ($\rho^{mol}(\mathbf{r})$), and isolated substrate ($\rho^{sub}(\mathbf{r})$).

$$\Delta\rho(\mathbf{r}) = \rho^{mol/sub}(\mathbf{r}) - \rho^{mol}(\mathbf{r}) - \rho^{sub}(\mathbf{r}) \ . \tag{3.5}$$

With the frozen adsorbed geometries, both $\rho^{mol}(\mathbf{r})$ and $\rho^{sub}(\mathbf{r})$ were achieved.

Here, an investigation of the local density of states (LDOS) and d-band centers is included. LDOS measures the density of electronic states in a material within a given

energy range, focusing on the states of the d orbitals in this context. The center of the d band indicates the average position of the d band relative to the Fermi energy. Given that ρ_{db} is the density of the d-band and E_{db} is the d-state energy, the d-band center is calculated by the first moment, as referenced in 3.6.

$$\frac{\int \rho_{db} E_{db} dE_{db}}{\int \rho_{db} dE_{db}}. \tag{3.6}$$

Part II

Results and Conclusions

4

Single-atom Rh-dopant Effects on the Adsorption Properties of Stepped Ag(211) Surfaces

This Chapter is presents the results obtained in the first article resulting from this thesis (DOI: 10.1039/D2CP04376A) [2]. It is separated into two topics, namely, (i) effect of Rh-dopants in the clean Ag(211) surface and (ii) adsorption properties of OH and CO.

4.1 Clean and Doped Surface

Firstly, the calculations for gas-phase molecules are presented in this section. The calculated bond lengths (d_0) of the isolated diatomic molecules are 0,98 Å (OH) and 1,14 Å (CO), differing by 1,1 % from the values reported in the literature [71]. Furthermore, we obtained binding energies of 4,75 eV/molecule for OH and 11,63 eV/molecule for CO, which match previous computational PBE results, [51, 72], with discrepancies of 0,42 % and 0,26 %, respectively.

Regarding the relative energy and ECN, we present the key results on the characteristics of pure Ag(211) and compare them with surfaces doped with Rh at different positions in Table 4.1. The Rh atom dopant is most energetically favorable at the corner chain. Energetically, the corner chain is approximately 0,50 eV more stable than the step and about 0,16 eV more stable than the terrace. This positional preference is associated with the site's ECN. The data indicate that the Rh dopant at sites with higher coordination and less exposure to vacuum has a lower energy configuration.

Table 4.1: Energetic, structural, and electrical features of Rh-doped Ag(211) and non-doped (in parentheses) surfaces. The relative energy of the different doping sites (ΔE_{tot}), work function (φ), and d-band center (ϵ_d), are given in eV, while effective coordination number (ECN) and the effective Bader charges are given in NNN and e, respectively.The work function of the clean Ag(211) surface is 4,20 eV.

System	ΔE_{tot}	ECN^{Rh} (ECN^{Ag})	φ	Q_{eff}^{Rh}	ϵ_d^{Rh} (ϵ_d^{Ag})
Step-Rh@Ag(211)	0.49	7.77 (7.13)	4.32	0.21	−3.08 (−4.05)
Terrace-Rh@Ag(211)	0.16	9.59 (8.97)	4.26	0.19	−3.32 (−4.14)
Corner-Rh@Ag(211)	0.00	10.52 (9.90)	4.21	0.21	−3.31 (−4.19)

Due to geometric relaxation reducing the atomic distances between the Rh dopant and the nearest neighbor Ag atoms, the ECN^{Rh} values for all dopant sites are higher than the corresponding Ag values in the absence of a dopant. For instance, on the non-doped surface, the shortest Ag-Ag distance is 2,81 Å, while the shortest Rh-Ag distance is 2,72 Å. Similarly, another study found that substituting a single Rh atom in stepped copper surfaces led to a decreased tendency for segregation energy as the coordination number of the Rh dopant increased [73].

The discussion now shifts to the work function and effective charges. The work function was found to be 4,20 eV for the pristine Ag(211) surface, consistent with previous DFT-PBE+vdW results (4,20 eV). However, self-consistent vdW adjustments ($\text{sc-vdW}^{\text{surf}}$) result in an increase in the work function to 4,59 eV [74, 75]. The largest difference between non-doped and Rh-doped surfaces occurs in the stepped configuration, amounting to 0,12 eV. This difference diminishes to a negligible value at the lowest energy structure (corner position).

The Bader charge analysis was conducted, revealing that Q_{eff}^{Rh} is positive, indicating an effective electron transfer from the surrounding Ag atoms. This aligns with the observation of electronegativity difference between the two elements [76]. As depicted in Figure 4.1, electron donation to the Rh atom occurs from the Ag atoms in the subsurface, while the silver atoms exposed to the vacuum remain largely unchanged. Table 4.1 corroborates that the charge on the Rh atom undergoes only minimal changes among dopant positions and is independent of ECN.

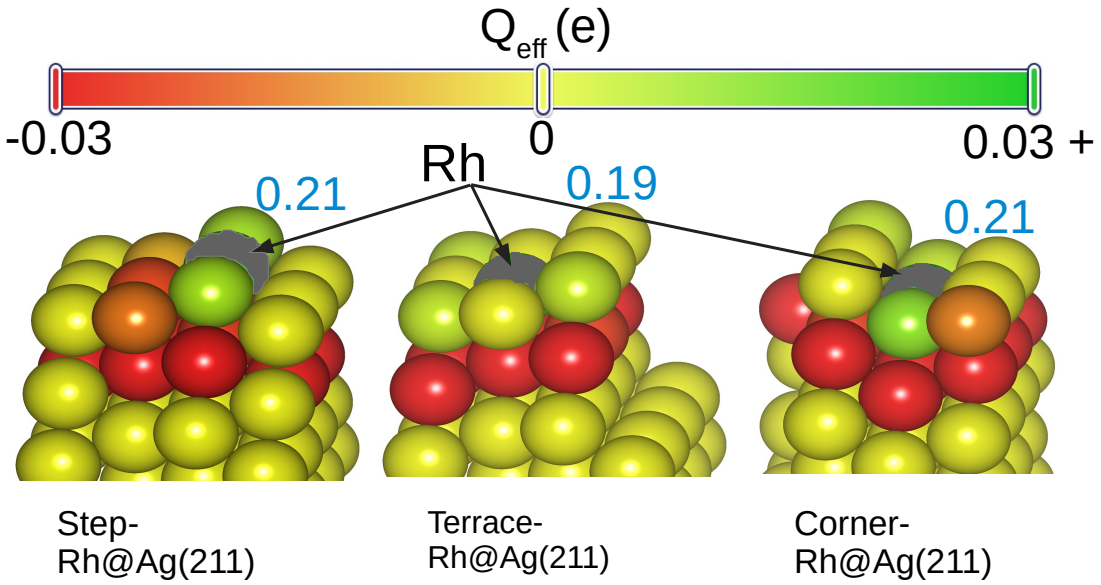


Figure 4.1: Bader charges for the Ag atoms in the doped surfaces. Q_{eff} gradient bar refers to Ag atoms only, while the Rh charges are given in the numbers in blue. e is the elementary charge, with a value of 1.6×10^{-19} coulomb. Reproduced from Ref. [2] with permission from the Royal Society of Chemistry.

Figure 4.2 illustrates the LDOS contribution of the Rh atom to the *d*-states in the step, terrace, and corner chains for step-Rh@Ag(211), terrace-Rh@Ag(211), and corner-Rh@Ag(211), respectively. For comparison, the *d*-states contribution from the Ag atoms at the same locations on the Ag(211) surface is also depicted. In all Rh-doped systems, Figure 4.2 reveals sharp peaks near the Fermi level. These distinct peaks identified in single-atom doped Ag(211) surfaces could result from a modest electronic density mixing between the Rh and Ag(211) atoms [77]. Additionally, the resemblance between such peaks and the DOS of the Rh atom in the gas-phase has been proposed as a potential explanation for the high reactivity of single-atom alloys [77, 78].

The *d*-band center values (ϵ_d) depicted in Figure 4.2 and summarized in Table 4.1 exhibit a notable shift towards the Fermi level due to the presence of single Rh atoms. This shift, along with the sharp localized peak near the Fermi level observed upon dopant substitution at all calculated positions, suggests a consistent trend across all substitution sites. Additionally, we observe an increase in *d*-band center values corresponding to a decrease in coordination of the surface atoms, a phenomenon even evident in non-doped Ag(211) surfaces; however, these changes are considerably smaller compared to those induced by the presence of the Rh dopant.

4.2 Adsorption Properties

Numerous configurations of adsorbed OH and CO were optimized for both doped and non-doped calculations, with many of them converging to the same local minimum.

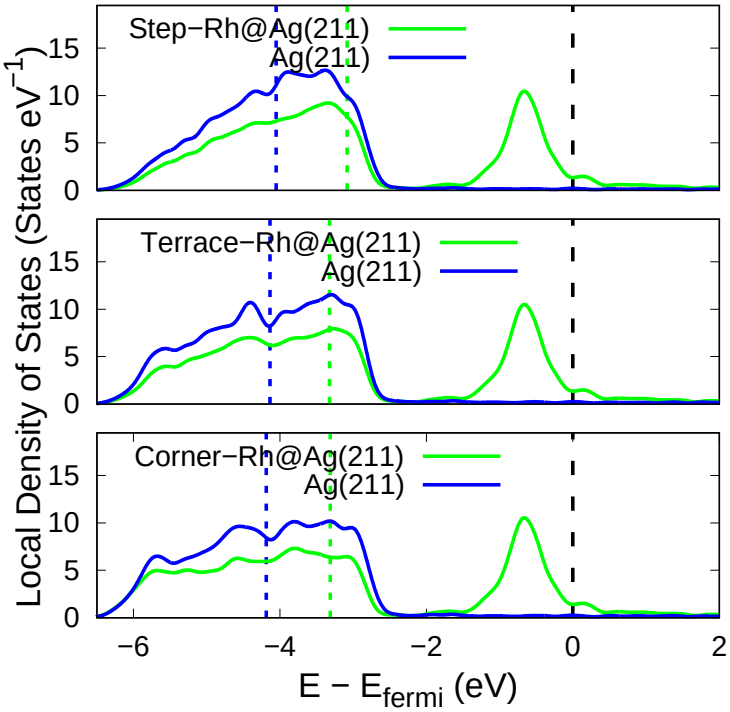


Figure 4.2: Local density of states (d-states contribution) for the non-doped and Rh-doped (step, terrace, and corner) Ag(211) surfaces. Comparing, the LDOS was calculated for the Rh and the replaced Ag atoms, respectively. The d-band centers are indicated by vertical lines, while the vertical dashed line at zero energy indicates the Fermi energy. Reproduced from Ref. [2] with permission from the Royal Society of Chemistry.

Figures 4.3 and 4.4 depict the top and side views of these structures, accounting for equivalences, for non-doped and doped surfaces, respectively.

This section correlates energy, distance, and coordination with the positions of the probe molecules following geometry optimization calculations. Figure 4.5 presents a summary of the results, arranged from the location where the dopant exerted the most significant influence on the adsorption energy (highest ΔE_{ad}) to the least. Additionally, the shortest metal-molecule lengths for each site are illustrated in Fig. 4.5.

Beginning with the OH/Rh@Ag(211) system, It is evident that the presence of the dopant atom significantly reduces the molecule-metal distances, indicating stronger interactions. This is supported by comparing the E_{ad} on doped and non-doped surfaces. The larger TM-O distances, comparable to those of the non-doped surface, clearly delineate the three cases in which the molecule is bound to a site far from the dopant (the x-axis of this graph also indicates if the molecule is not bound to Rh by specifying which metal atoms are involved in the adsorption in parentheses). As expected, the adsorption energy for doped and non-doped cases is relatively similar in such instances.

More silver atoms are in proximity to the probe molecule when it is adsorbed on hollow hcp or fcc sites. Consequently, their influence implies that the introduction of the

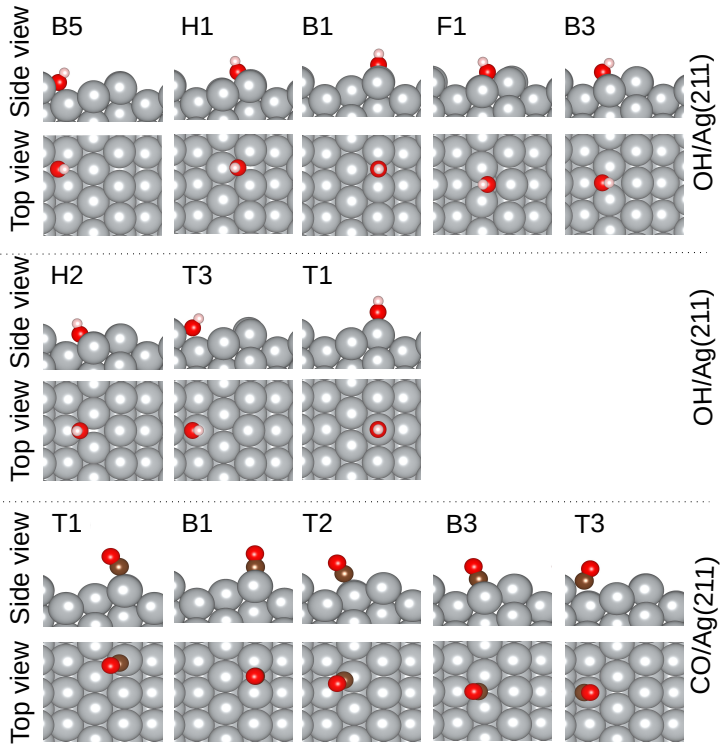


Figure 4.3: Top and side view of the adsorption configurations for OH and CO on Ag(211). The label above each structure represents the adsorption site. Ag is grey, O is red, C is brown and H is light pink. Reproduced from Ref. [2] with permission from the Royal Society of Chemistry.

single-atom dopant does not markedly alter the energy. This differs from the scenario when the occupied sites are atop or bridge positions. The inclusion of the single-atom dopant redirects the adsorption preference away from the bridge and hollow Ag sites towards top and bridge sites containing Rh atoms. The T1-step configuration, weakest in adsorption on the non-doped surface, exhibits the highest ΔE_{ad} value, while the B1-step configuration represents the strongest adsorbed configuration. It is noteworthy that all E_{ad} values fall within the chemisorption range. The strongest adsorptions, as indicated by E_{ad}, occur with the dopant in the step position.

The behavior of CO differs. It exclusively binds to the dopant on top sites, resulting in just one configuration for each dopant location. The surface-molecule distance is significantly smaller in these cases compared to when the molecule is adsorbed on Ag. Examination of the adsorption energies reveals that CO interactions with Ag represent physisorption, while interactions with Rh correspond to chemisorption. Adsorption energies are minimal and very similar to the non-doped scenario when the molecule is not situated on a top site above the dopant (as indicated by the small magnitude of ΔE_{ad}). The presence of the sharp localized peak on d-states contribution for the LDOS curves and the upward shift of the d-band center, previously correlated with stronger adsorption of various molecules on metallic surfaces, can be associated with the enhanced

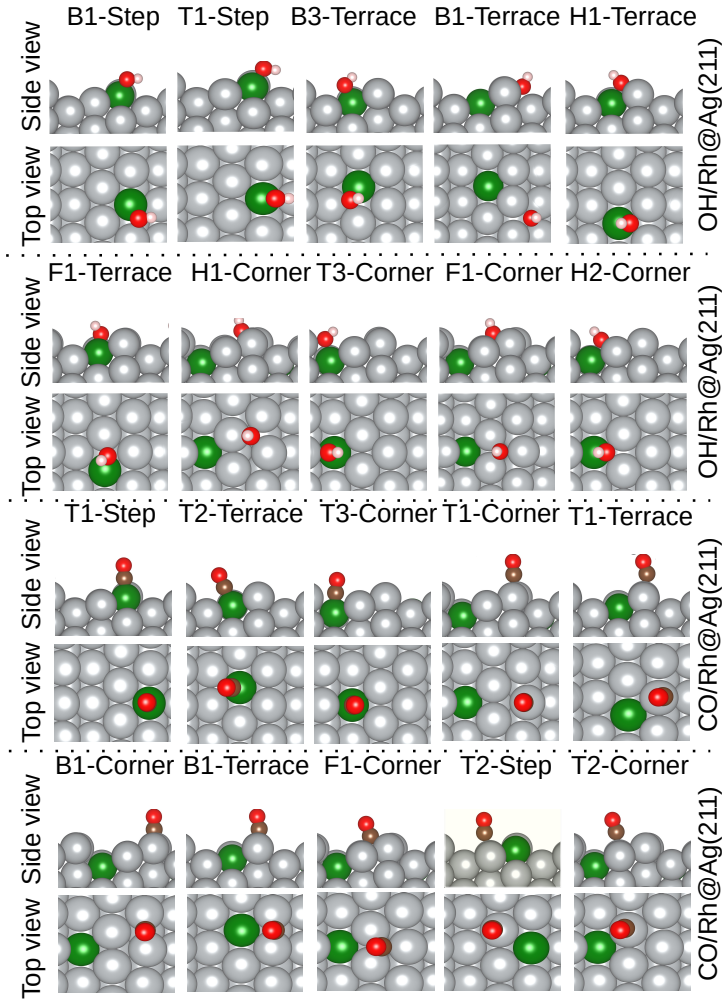


Figure 4.4: Top and side view of the adsorption configurations for OH and CO on Ag(211) doped with Rh. The label above each structure represents the adsorption site followed by the chain in which the dopant lies. Rh is shown in green, Ag in grey, O in red C in brown and H in light pink. Reproduced from Ref. [2] with permission from the Royal Society of Chemistry.

adsorption energies near Rh sites observed in this section for both molecules [77]

The Gibbs free energy of adsorption was computed for the lowest energy structures of doped and non-doped surfaces (CO/Ag(211) on T1 and CO/Rh@Ag(211) on T1-step). We found that $G_{ad} = 0{,}56\,\text{eV}$ for the non-doped surface and $G_{ad} = -1{,}33\,\text{eV}$ for the doped surface. Consequently, our calculations suggest that weakly bound CO adsorption on non-doped Ag(211) will not be spontaneous, consistent with previously published results [79]. However, the introduction of a single atom dopant alters this scenario. The greater adsorption energy (chemisorption) is the primary reason for this difference, as the other contributions to G are similar in both doped and non-doped surfaces.

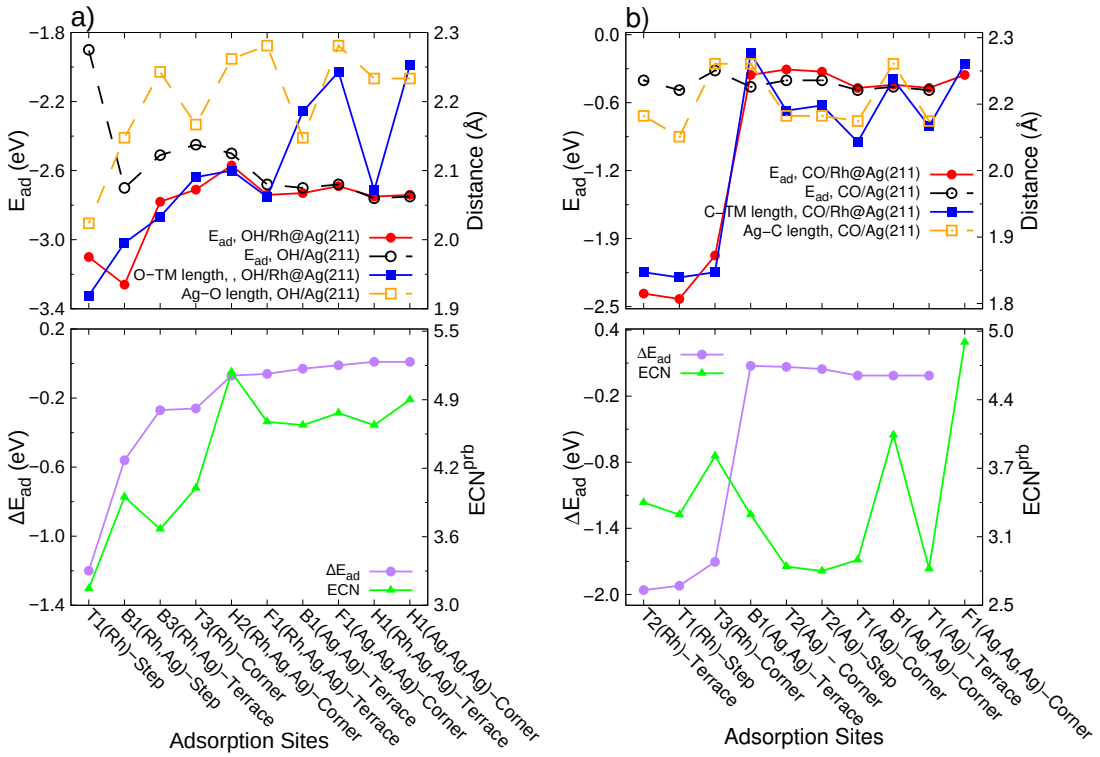


Figure 4.5: Geometric parameters and adsorption energies for the a) OH/Rh@Ag(211) and b) CO/Rh@Ag(211) systems. The elements in parenthesis represent to which atoms of the doped surface the molecule is bound to. Reproduced from Ref. [2] with permission from the Royal Society of Chemistry.

4.2.1 Geometric Parameters

Figure 4.5 illustrates the ECN of the probe molecule (ECN^{prb}), considering only the atom closer to the surface: O for the OH molecule and C for CO. This facilitates a more quantitative discussion, as positions near the corner typically exhibit higher coordination if the molecule can also bond to atoms in the subsequent step, which the labels top, bridge, and hollow do not encompass.

In the case of OH, which exhibits stronger adsorption as detailed in the preceding section, it was observed that the impact of a single Rh atom on modifying the adsorption energy (ΔE_{ad}) depends on the coordination of the O atom, as assessed by ECN^{prb}. ECN^{prb} is significantly lower in the four instances where ΔE_{ad} was substantial ($> 0{,}2\,eV$) compared to other sites. In other words, adsorption sites adjacent to the dopant with lower coordination of the O atom show a more pronounced change in energy, likely due to the molecule's inclination to bond more directly to the single dopant with fewer interactions with neighboring Ag atoms.

For carbon monoxide, a larger ECN^{prb} is observed, focusing solely on the three top configurations where the molecule is directly bonded to the dopant. This is because the chemisorbed Rh-C distance is less than the Ag-C distance. Peaks for bridge and hollow

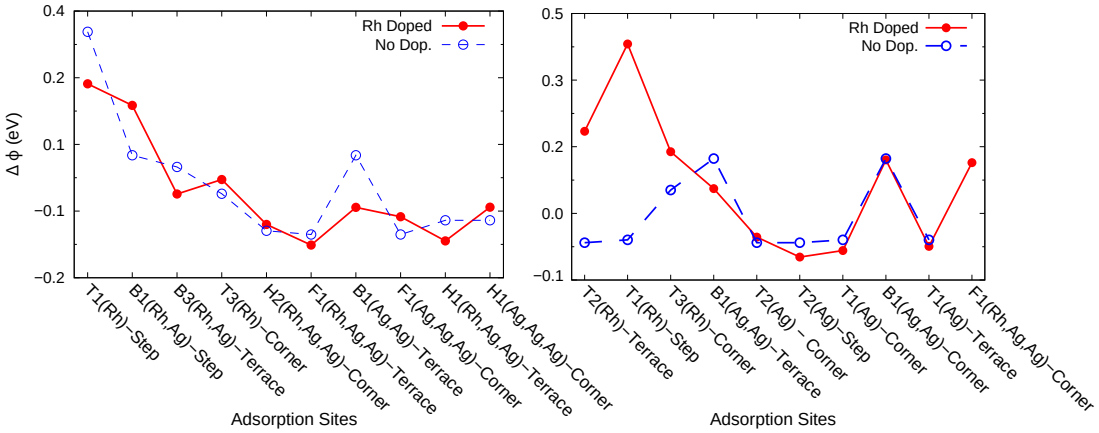


Figure 4.6: Work function difference induced by the presence of the molecules on doped and non-doped surfaces for OH (left panel) and CO (right panel). Reproduced from Ref. [2] with permission from the Royal Society of Chemistry.

configurations are evident for instances where the molecule is adsorbed solely on silver atoms; however, these fall within the physisorption range and have no impact on ΔE_{ad}.

4.2.2 Work function Change and Electron Density Difference

The change in the work function induced by the presence of the probe molecules ($\Delta\varphi^{mol/surf} - \varphi^{surf}$) is illustrated in Figure 4.6, organized in the same manner as the preceding figures (decreasing ΔE_{ad}). We observed that the impact of OH on both doped and non-doped surfaces is relatively similar, with a modest change ranging from $-0{,}10$ to $0{,}10\,\text{eV}$ in most cases. A change exceeding $0{,}10\,\text{eV}$ was exclusively observed for the doped case when both the molecule and dopant were situated at the step chain, the two configurations with the largest E_{ad} modulus, indicating that the presence of the molecule renders the surface more electrically stable. It is worth noting that a similar trend was observed when examining the effect of the dopant on the work function (greatest change with the dopant on the step chain). Only the T1 configuration (lowest E_{ad} modulus) exhibited a noticeable change on the non-doped surface.

The behavior of doped and non-doped surfaces is not as similar for the CO molecule, and we focus on the three examples when the molecule is linked directly to the Rh atom. Remember that these are the only three examples where the carbon monoxide molecule is chemically adsorbed (the CO – Ag interaction indicated physisorption). This shows that the surface is stabilized by a chemical link formed between CO and Rh. it is also worth noting that when the molecule only attaches to Ag atoms, bridge, and hollow structures have a positive $\Delta\varphi$ value, whereas top sites have a negative one. This demonstrates an intriguing relationship with ECN^{prb} as can be seen in figure 4.5.

The behavior of doped and non-doped surfaces diverges more noticeably for the CO molecule, particularly when the molecule directly binds to the Rh atom. It is important to note that these instances represent the only scenarios where the carbon monoxide molecule

undergoes chemical adsorption, as the CO – Ag interaction indicates physisorption. This suggests that the surface stability is enhanced by the chemical bond formed between CO and Rh. Additionally, when the molecule solely attaches to Ag atoms, bridge and hollow structures exhibit a positive $\Delta\varphi$ value, whereas top sites display a negative one. This intriguing relationship with ECN^{prb} can be observed in Figure 4.5.

The electron density differences for all adsorption configurations observed on the doped surface are given in Figure 4.7. We found a significant rise in electron density surrounding the molecule and a reduction just above the surface for OH, confirming a surface-molecular electron transfer during adsorption. These findings can be explained by noting that the Bader charge analysis revealed that the Rh atom pulls electrons from the subsurface, in the absence of a molecule, making it negatively charged and available for such electron donation. In the case of carbon monoxide, a separate mechanism may be shown in the three circumstances when the molecule is directly linked to the dopant, previously proven to be the cases where CO chemically attaches to the surface. In the C-Rh bond area, there is a significant accumulation of electron density. The surface does not display an electron density loss, as in the case of OH, and this electron transfer appears to occur from the subsurface to the newly formed bond. The Rh atom, which was already negatively charged prior to adsorption, becomes considerably more so after adsorption. Interestingly, the electron density in the carbon-oxygen bond itself is diminished, indicating that the molecule is being activated and would be more easily disrupted in a catalytic process.

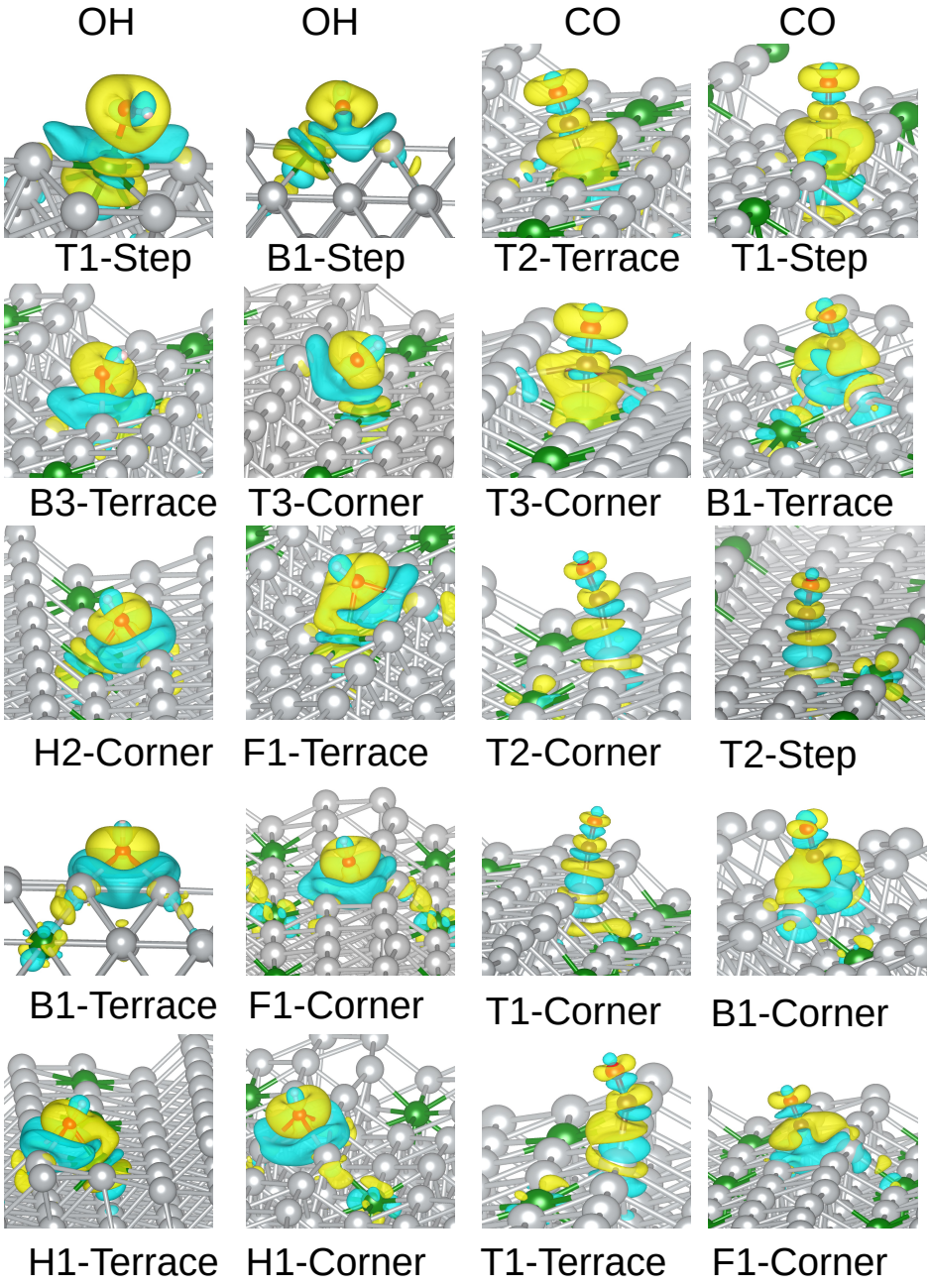


Figure 4.7: Electron density difference. (0.0014 eÅ^{-3}) for CO and OH adsorbed on Ag(211) doped with Rh. The label for the sites follows the ones defined in the text. Yellow and blue colors show accumulation and depletion of charge, respectively. Reproduced from Ref. [2] with permission from the Royal Society of Chemistry.

5

Computational Screening of Silver-based Single-atom Alloys Catalysts for CO_2 Reduction

This Chapter presents the results obtained in the second article resulting from this thesis (DOI: 10.1063/5.0192055) [1]. It is separated into two topics, namely, (i) Effects of structural and electronic properties when applying dopants to Ag(211). (ii) Analysis of the adsorption of reaction intermediates and screening for performance evaluation of substrates as SAAC.

5.1 TM@Ag(211) Surfaces

Table 5.1 displays the geometric and energetic parameters for all selected substrates. For doped surfaces, values for the adjacent Ag surface atom to the dopant are also provided (in parentheses). It is worth noting that all dopants exhibit greater energetic stability when located at the more coordinated terrace site. Among lighter metals serving as dopants (Fe, Co, Ni, and Cu), the energy difference between these two possibilities is marginal, whereas for Rh and Ir, a more significant alteration is evident.

Naturally, the ECN of atoms on the terrace exceeds that of those at the step positions. It is worth noting that among all the chemical elements considered in this study, Ag shows the largest metallic radius. Consequently, Ag–Ag bonds are longer compared to TM-Ag bonds, elucidating the lower ECN observed for the non-doped surface, as illustrated in Table 5.1. Conversely, the presence of a dopant extends the neighboring Ag–Ag bonds on the doped surface, resulting in a reduction in ECN at the silver atom adjacent to the TM dopant site, relative to the values for the non-doped surface.

Analysis of the distance ($d^{\mathrm{TM-Ag}}$) between TM and silver atoms (considering only surface Ag atoms) reveals that dopants positioned at the step tend to be closer to a silver atom than when the dopant is situated at the terrace. Across all single-atom additions achieved, the dopant in the step configuration exhibits closer proximity to Ag on the terrace, while the dopant in the terrace configuration demonstrates the closest proximity to Ag at the corner.

One suggested explanation for the unique catalytic behavior of SAACs is their

Table 5.1: Properties of the non-doped and TM-doped Ag(211) surfaces. The relative energy between dopant sites (ΔE_{tot}) is given in eV, effective coordination numbers (ECN) are given in number of nearest neighbors (NNN), d-band center (ϵ_d) in eV, and shortest distance between Ag and dopant atoms in the surface ($d^{\mathrm{TM-Ag}}$) in Å. The values in parentheses correspond to the results for the silver atom exposed to the vacuum that is closest to the TM dopant.

TM-position	ΔE_{tot}	$\mathrm{ECN}^{\mathrm{TM}}$ ($\mathrm{ECN}^{\mathrm{Ag}}$)	ϵ_d^{TM} (ϵ_d^{Ag})	$d^{\mathrm{TM-Ag}}$
non-doped Ag@Step	-	7.13	−4.05	-
non-doped Ag@Terrace	-	8.97	−4.14	-
Fe@Step	0.04	7.66 (7.00)	−0.47 (−3.92)	2.78
Fe@Terrace	0.00	9.67 (8.84)	−0.55(−4.02)	2.81
Co@Step	0.16	8.00 (6.84)	−0.56(−4.00)	2.70
Co@Terrace	0.00	9.52 (8.88)	−0.58 (−4.07)	2.82
Ni@Step	0.20	8.24 (6.75)	−0.79 (−3.98)	2.66
Ni@Terrace	0.00	9.80 (8.80)	−0.85 (−4.08)	2.79
Cu@Step	0.10	7.96 (6.87)	−2.09 (−4.03)	2.70
Cu@Terrace	0.00	9.61 (8.86)	−2.14 (−4.11)	2.78
Rh@Step	0.33	7.77 (6.92)	−1.15 (−3.89)	2.75
Rh@Terrace	0.00	9.59 (8.85)	−1.30 (−4.04)	2.80
Ir@Step	0.43	7.92 (6.81)	−1.27 (−3.87)	2.73
Ir@Terrace	0.00	9.67 (8.82)	−1.43 (−4.03)	2.80

restricted mixing of the host and dopant wave functions, resulting in clearly defined electronic states similar to those of 'free atoms'. This occurrence, as documented in previous research [2, 77, 80], leads to an increase in electronic states near the Fermi energy and subsequently causes an upward shift in the d-band center. Accordingly, Table 5.1 presents the d-band center values for all substrates, while their corresponding local density of states (LDOS) is depicted in Figure 5.1. Clearly, novel peaks emerge near the Fermi energy on doped surfaces, a characteristic not found on pristine surfaces.

Moreover, it is evident that across all substrates, atoms positioned at step sites tend to have their d-band centers situated slightly nearer to the Fermi energy compared to those on terrace sites [81]. It is worth mentioning that the adsorption energy on metallic surfaces is known to be correlated with the d-band center [82, 83]. When investigating dopants from the fourth period (Fe, Co, Ni, Cu), a pattern emerges: a higher number of valence electrons corresponds to a d-band center farther away from the Fermi energy. Specifically, Fe displays the peak closest to the Fermi energy, whereas Cu exhibits the one nearest to non-doped silver. Interestingly, Rh and Ir showcase notably similar LDOS profiles, resulting in closely aligned d-band centers.

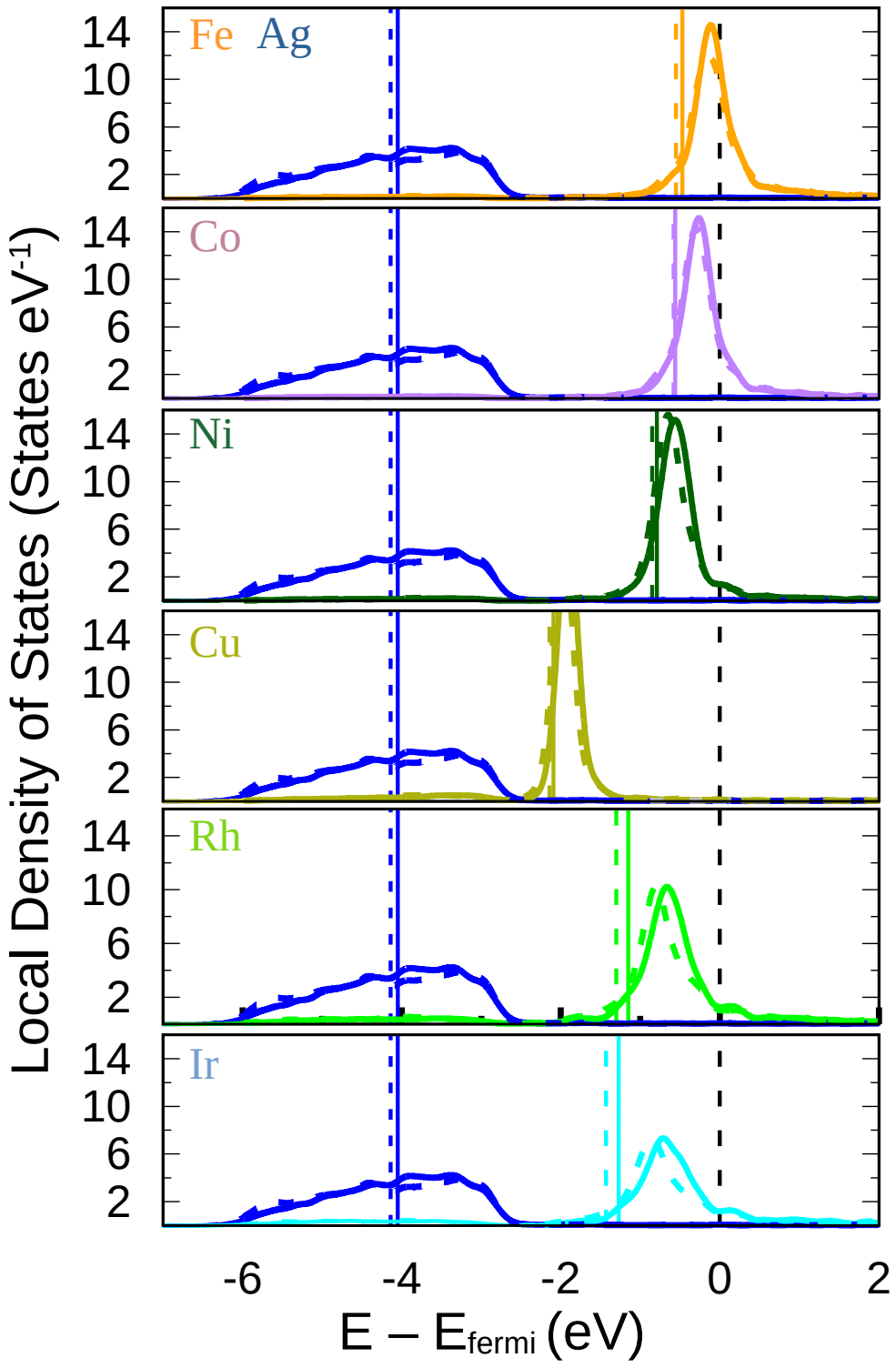


Figure 5.1: Local density of states along with the *d*-band center analyses for single-atoms at the step (solid line) or terrace positions (dashed). Blue curves correspond to the non-doped Ag(211) surface, while the remaining colors correspond to the doped surface. The *d*-band centers are indicated with colored vertical lines, while the Fermi energy is indicated by a vertical black dashed line. Reproduced from [1], with the permission of AIP Publishing.

5.2 Adsorption of CO_2RR Intermediates

For this analysis, the lowest energy configurations for each surface and molecule were considered, indicating that different sites were explored in the search for the lowest energy. The step and terrace sites were chosen because they represent different environments and coordinations on the catalyst surface. Starting with the non-doped Ag, as shown in Figure 5.2, it becomes evident that molecules display a preference for sites with lower coordination near the step. While OH appears to deviate from this trend, the lowest energy site depicted in this figure is nearly degenerate with a hollow site near the step, with the energy difference falling below the expected accuracy of the calculations. Species containing carbon (CO, COH, and CHO) bind to the surface via carbon and tend to favor the top and hollow sites. Additionally, we present in Figure 5.2 the E_{ad} of each configuration, calculated using equation 3.4.

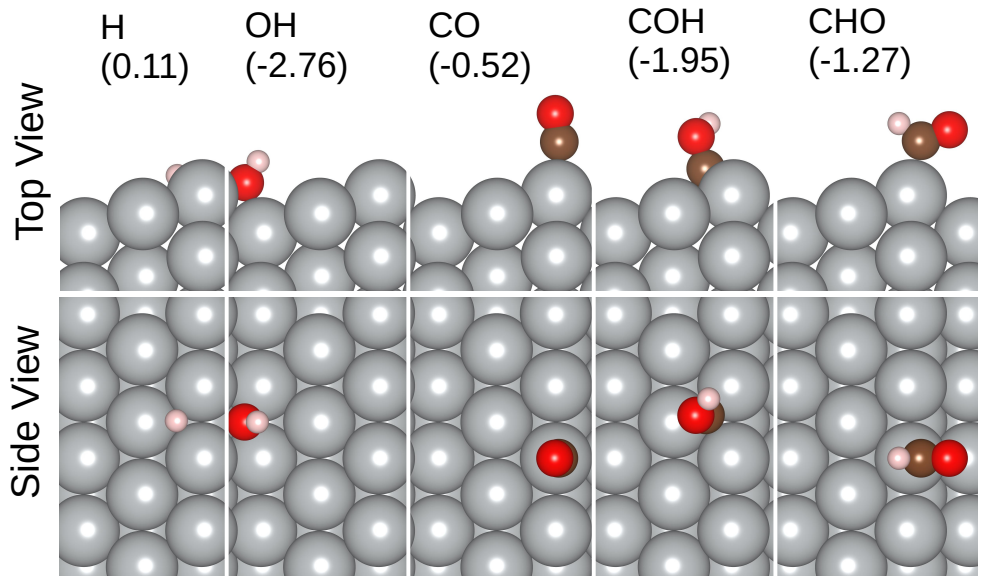


Figure 5.2: Top and side view of the lowest energy adsorption configurations on Ag(211). The adsorption energy is given eV. Ag is gray, O is red C is brown and H is light pink. Reproduced from [1], with the permission of AIP Publishing.

As previously documented [84], OH displays robust binding to the noble metal surface, while CO exhibits a weak physisorption interaction, contributing to the easy desorption of CO in the CO_2RR when silver is utilized as an electrode [46]. Conversely, for hydrogenated species such as COH and CHO, the adsorption energies shift towards chemisorption. Figure 5.3 illustrates the adsorption configurations for the dopants in the step and terrace cases. It is evident that hydrogen atoms adsorb on bridge and hollow sites, except for the Ir case, which displays significantly higher values for E_{ad} and a preference for adsorption at the top site. The Cu dopant exhibits weaker H adsorption similar to the behavior of non-doped silver (both being coinage metals), possibly due to its LDOS peak being farther from the Fermi energy. Notably, for atomic hydrogen, the magnitude of the adsorption

energy consistently increases when the dopant is positioned in the step position.

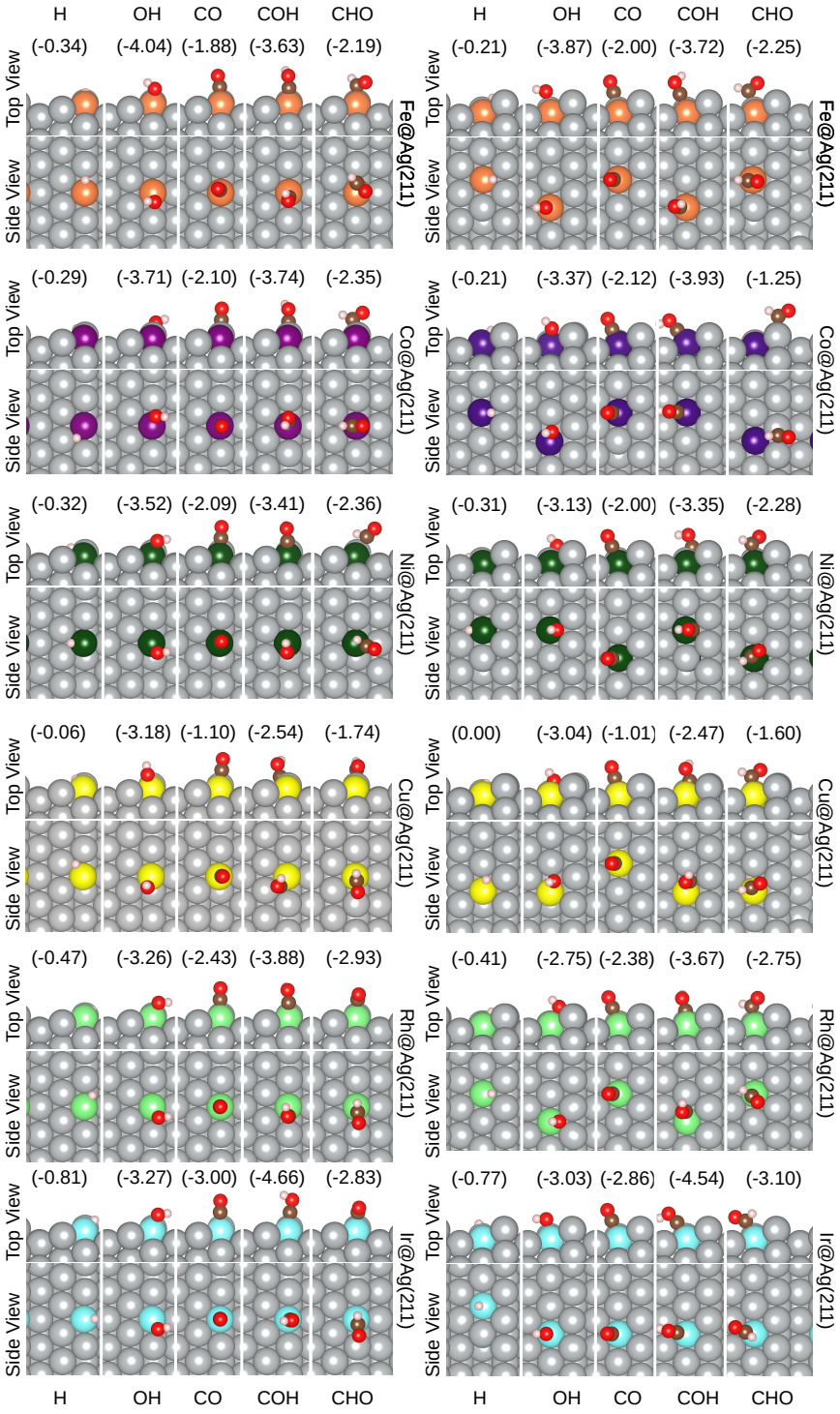


Figure 5.3: Top and side views for the minimum energy adsorption configuration of each system with the TM Dopant on the step position (left) and terrace position (right). Adsorption energy is given in parenthesis. Reproduced from [1], with the permission of AIP Publishing.

While the OH molecule displays stronger binding to dopants positioned in the step configuration, it diverges from the hydrogen atom in that it does not exhibit a stronger affinity for heavier metals (Rh and Ir). Surprisingly, it binds more strongly to iron, and the values of E_{ad} correspond to the trend of the d-band center of the transition metal. Consequently, we can infer that the iron-doped surface is prone to poisoning by OH.

The examination here focuses on the behaviors of H and OH species for potential competing mechanisms, while the involvement of the CO molecule in the CO_2RR is a topic of discussion. This closed-shell molecule consistently adsorbs at the top sites of the dopant atom, with binding strength not linearly correlated with its d-band centers. Similarly to the case of H, the heaviest metals exhibit higher magnitudes of E_{ad}. Interestingly, on the Fe-doped surface, we observe the first instance where the dopant in the terrace position adsorbs more strongly than in the step position (a similar observation occurs for CO on the Co-doped surface, although the difference in adsorption energy lies below the accuracy of the calculations).

The initial hydrogenation step subsequent to CO adsorption involves proton-coupled electron transfer to produce COH or CHO. As depicted in Figure 5.3, we observe a behavior similar to that of CO, wherein adsorption on the doped surfaces of Fe and Co is weaker in the step position. Similar to H and CO, adsorption is notably stronger on heavier metals (Rh and Ir). Remarkably, no CHO adsorption was achieved on the Co-doped surface on the terrace (geometry optimizations initiated from this configuration resulted in dissociation towards CO + H), resulting in an adsorption energy very close to the non-doped silver case.

Figure 5.4 depicts the relationship between the free energies of formation (relative to a clean surface and gas phase H_2 and CO) among adsorbed species, enabling us to pinpoint potential cases that deviate from the anticipated linear scaling relationships. Initially, although the CHO adsorbed on the Co@Ag(211)-terrace evidently diverges from the others, it is crucial to note that in this specific instance, the molecule is adsorbed far from the dopant (see Figure 5.3). Consequently, this value is not included in the fitting procedure. The graph indicates that the formation of CHO is favored over COH, but the fitted line predicts a reversal of this trend for surfaces binding CO very strongly, as demonstrated by Karamad et al [85]. It is important to underscore that these results do not reflect adsorption energies, where gas phase CHO and COH molecules serve as references.

A catalyst with the ability to enhance activity by disrupting the linear scaling relationship would stabilize *CHO formation without a corresponding stabilization of *CO, thus promoting the *CO $\longrightarrow$ *CHO step. This is illustrated in the graph by a point located below the trend line. From this perspective, we can observe the Rh-step configuration as an interesting instance of breaking the linear trend in favor of *CHO. Equally notable is the Co dopant in the terrace site, which interrupts the linear scaling for the *COH molecule.

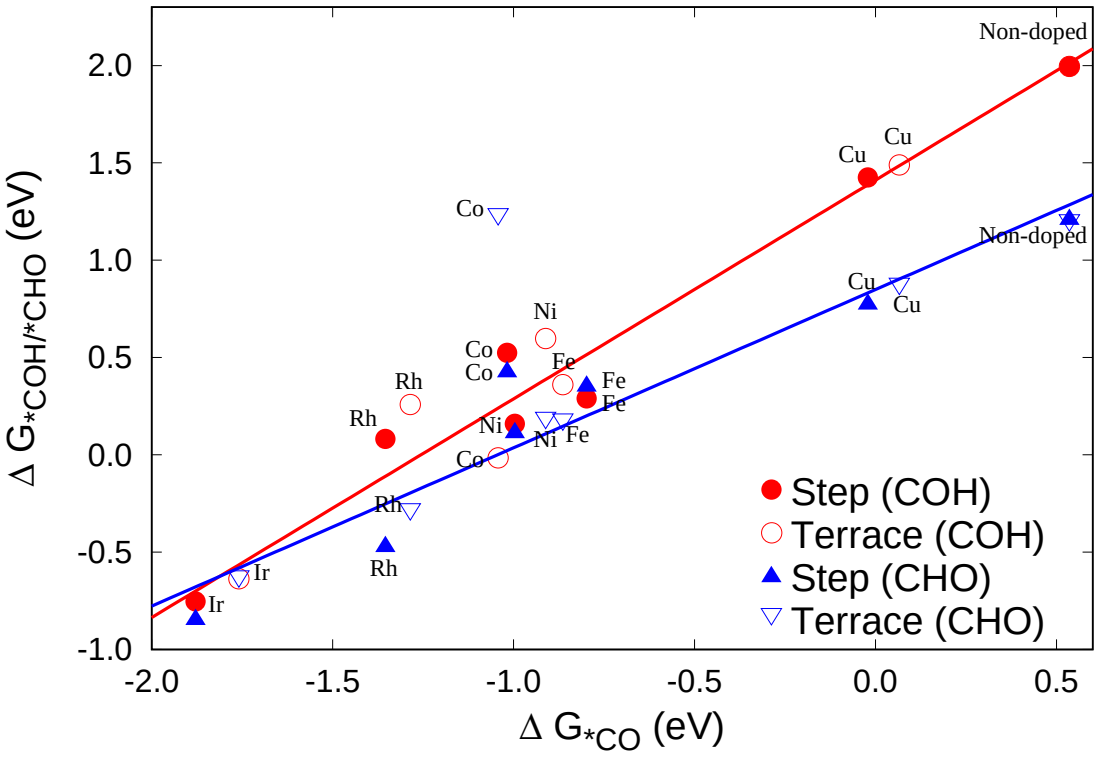


Figure 5.4: Free energies of formation (relative to a clean surface, and gas-phase H_2 and CO) between the adsorbed species. The lines represent the fitted data for each molecule separately. Reproduced from [1], with the permission of AIP Publishing.

5.3 Screening of TM/Ag(211) Single-atom Alloy Catalyst for CO_2RR

At the minimum energy configuration achieved for the interaction between each molecule and substrate, a harmonic vibrational analysis was conducted to calculate the Gibbs free energy, as outlined in equation 2.55. Figure 5.5 illustrates the Gibbs free energy diagrams according to the Computational Hydrogen Electrode (CHE) model for selected steps of the CO_2RR. It is important to note that within the CHE model, the change in free energy in the Proton-Coupled Electron Transfer (PCET) step from *CO $\longrightarrow$ *COH/CHO is calculated as $G_{*\mathrm{COH/CHO}} - G_{*\mathrm{CO}} - \frac{1}{2}G_{\mathrm{H_2}}$. The figure is divided for substrates where the dopant atom is positioned in the step or terrace location. Side panels are included to illustrate competing processes (HER and poisoning by OH): for G_{HER}, a significantly positive value indicates suppression of HER (as intended), while $G_{\mathrm{OH-H_2O}}$ should be minimal (or smaller than the potential determining step) for OH to spontaneously vacate the active sites and avoid poisoning the catalyst.

Based on our premise, the higher abundance of Ag atoms facilitates the transformation of CO_2 into CO, which then binds more strongly to the dopant due to its enhanced interaction [86]. This is succeeded by either CO desorption or the initial Proton-Coupled

Electron Transfer (PCET) step. Therefore, the figure employs adsorbed CO as a reference energy, allowing for straightforward comparison of the free energy of both competitive processes. For example, the Cu-doped surface closely resembles non-doped silver, where desorption occurs spontaneously, suggesting it may not be an ideal catalyst candidate. Indeed, this Single Atom Alloy Catalyst (SAAC) even promotes the Hydrogen Evolution Reaction (HER) compared to non-doped silver. Regarding water formation, while the non-doped surface can release the OH radical spontaneously towards water formation, the Cu-doped surface requires an applied potential to surpass the endoergic nature of this step; otherwise, its active sites would be poisoned by this species.

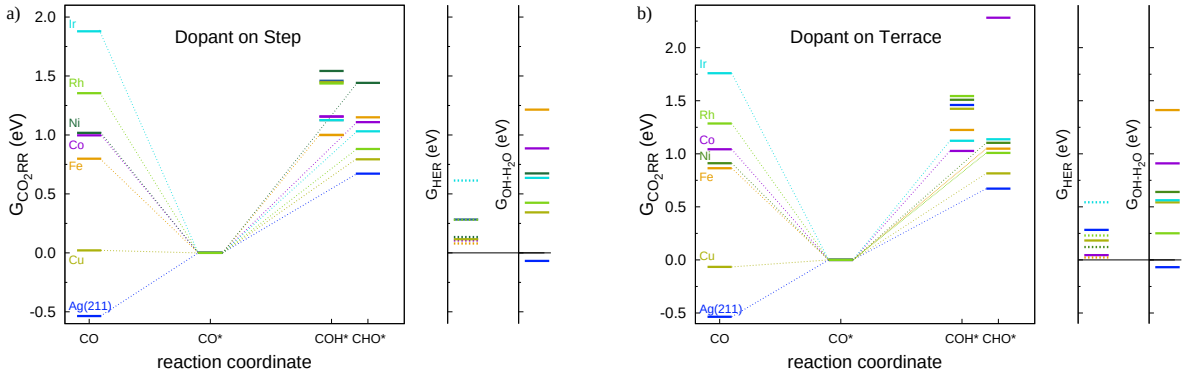


Figure 5.5: Free energy diagrams for non-doped silver and SAA surfaces with dopants on the step (a) and terrace (b) positions. The free energy for the competing HER and formation of H_2O from adsorbed OH are given as sidebars. In the HER diagram, the solid lines indicate that the potential determining step is the hydrogen adsorption, rather than its subsequent hydrogenation and desorption as H_2, which is shown in dash. Reproduced from [1], with the permission of AIP Publishing.

Generally, most substrates display a preference for CHO over COH, with certain exceptions such as Fe substitution at the step position, and Ir and Co at the terrace position. Notably, surfaces doped with the two heaviest metals (Ir and Rh) show a higher tendency to reduce *CO compared to desorbing it. Moreover, the Ir@Ag(211) surface necessitates significantly more energy for the Hydrogen Evolution Reaction (HER) compared to non-doped silver and even non-doped copper [21] (known for its ability to reduce CO_2 beyond CO with notable Faradaic efficiency), potentially reducing the overpotential required to suppress HER (compared to metallic copper). The Rh@Ag(211) surface also demonstrates an enhancement over copper in this aspect, albeit to a lesser degree than Ir.

When examining the *OH $\longrightarrow$ H_2O step, it becomes apparent that removing hydroxyl groups from the surface requires less energy compared to the CO_2RR, making it readily achievable under the applied potentials necessary for the reaction. Additionally, it is noteworthy that a lower applied potential is needed when the dopant is situated at a step, indicating that surface defects or the utilization of nanoparticles could further enhance these catalysts. Consequently, based on our calculations, the Ir@Ag(211) and Rh@Ag(211) SAACs emerge as the most promising candidates.

Among the elements belonging to the fourth period (Fe, Co, Ni, Cu), there is a tendency to prioritize CO desorption over hydrogenation towards CHO or COH which would lead to the production of more reduced products. However, Fe and Co are likely to enhance HER and are prone to OH poisoning. Notably, Fe@Ag(211) stands out as the only substrate where the removal of OH is more energetically demanding than the desorption or hydrogenation of CO. However, contrary to these findings, the iron dopant in analogous Cu(211) has been identified as one of the most promising catalysts in a previous computational study [87]. Overall, it is evident that none of the SAACs proposed here will significantly favor the reduction of CO over HER, a phenomenon also observed for non-doped copper, which is known to produce methane under sufficient overpotential.

6 Conclusion

In this study, we used DFT-PBE+D3 calculations to investigate the adsorption behaviors of OH and CO on Rh-doped and non-doped stepped Ag(211) surfaces. According to our calculations, the substitution of a single Rh atom in the Ag(211) surface causes a charge transfer from the subsurface to the dopant, which is accompanied by the emergence of a strong and unmistakable peak around the Fermi level in the density of states. The energy stability of the doped surface is proportional to the coordination number presented by the dopant Rh atom, with the most coordinated and least exposed to the vacuum locations exhibiting the lowest energies. This significantly altered the adsorption behavior of the two chemically different compounds investigated here.

The magnitude of the adsorption energy for OH was found to increase on the doped surface, accompanied by a decrease in the molecule-surface distance. When comparing identical sites on doped and non-doped surfaces, this effect was stronger for adsorption sites with a more coordinated oxygen atom (ECN^{prb}). Because of its unpaired electron, the OH molecule is more reactive than the CO molecule and chemically attaches to the silver atoms regardless of the presence of the dopant. Whereas OH prefers bridge and hollow sites in the Ag(211), the addition of the dopant shifts this to top and bridge sites. This is not the case with the CO molecule, which interacts with the noble metal surface only faintly. The addition of the Rh atom dopant, on the other hand, was capable of substantially altering this behavior, resulting in much greater adsorption energies and shorter surface-molecule distances. The favorable configurations on the doped surface are those with the CO molecule coupled only to the dopant at top configurations. This is an intriguing feature for single-atom catalysts, which are frequently driven by the energy difference between host and dopant sites. A higher magnitude of adsorption energy was obtained for both molecules when the dopant was in the surface's step chain, where it is most exposed to the vacuum and has a *d*-band center lying closer to the Fermi energy.

According to our findings, there is an electron transfer from the partially negative dopant atom to the molecule for OH, which may stabilize it by lowering the radical, unpaired electron, the character of this molecule. On the other hand, there appears to be a charge depletion from the subsurface to a newly created surface-molecule chemical connection during CO adsorption. A charge depletion of the carbon-oxygen bond happens

as well, indicating that the adsorption will make the molecule more susceptible to bond-breaking or reactive processes. With these results, it was possible to publish an article entitled Role of Single-atom Rh-dopants in the Adsorption Properties of OH and CO on Stepped Ag(211) Surfaces [2].

Also, calculations framework were integrated with the CHE model to identify single-atom substitution dopants for the host Ag(211) substrate, aiming to enhance the reduction of CO_2 toward the production of CH_4 and CH_3OH. Our calculations and analyses revealed the emergence of distinct peaks in the density of states of doped Ag(211) surfaces, indicative of a general electronic characteristic associated with poor mixing between dopants and the host substrate. While this effect was less pronounced when copper was employed as a dopant due to its electronic structure distribution resembling that of silver atoms, other dopants with incomplete *d*-band occupation exhibited significant electronic distribution alterations, thereby influencing the interaction of CO_2 reduction intermediates with the doped substrate and resulting in distinct reaction profiles.

Specifically, we demonstrated a transition from weak physisorption-type CO adsorption on the non-doped Ag(211) surface to strong chemisorption characteristics on doped surfaces, particularly when molecules bind on or near the dopant site. We observed a linear scaling relationship between the free energy of CO adsorption and that of COH and CHO, with only a few cases deviating from the general trend.

Elements from the fourth period (Fe, Co, Ni) exhibited stronger CO binding compared to coinage metals, yet our findings indicated that they did not favor its hydrogenation toward more reduced products. These lighter metals were also predicted to enhance the HER reaction. Notably, our calculations identified Ir and Rh as potential dopants for electrocatalysts, promoting CO reduction over desorption and suppressing the HER reaction, while being resistant to poisoning by OH radicals [1].

Bibliography

[1] M. M. Neto, L. G. Verga, J. L. Da Silva and B. R. Galvão, Computational screening of silver-based single-atom alloys catalysts for CO_2 reduction, *J. Chem. Phys.*, 2024, **160**, year, DOI: 10.1063/5.0192055.

[2] M. M. Neto, L. G. Verga, B. R. Galvão and J. L. Da Silva, Role of Single-atom Rh-dopants in the Adsorption Properties of OH and CO on Stepped Ag (211) Surfaces, *Phys. Chem. Chem. Phys.*, 2023, **5**, 31–35, DOI: 10.1039/D2CP04376A.

[3] V. C. H. C. Oliveira, B. L. Damineli, V. Agopyan and V. M. John, Estratégias para a minimização da emissão de CO2 de concretos, *Ambiente construído*, 2014, **14**, 167–181.

[4] G. T. da Silva, O. F. Lopes, E. H. Dias, J. A. Torres, A. E. Nogueira, L. A. Faustino, F. S. Prado, A. O. Patrocínio and C. Ribeiro, ReduÇÃo de CO 2 em hidrocarbonetos e oxigenados: Fundamentos, estrategias e desafios, *Química Nova*, 2021, **44**, 963–981.

[5] M. Crippa, D. Guizzardi, M. Muntean, E. Schaaf, E. Solazzo, F. Monforti-Ferrario, J. Olivier and E. Vignati, Fossil CO2 emissions of all world countries, *Luxembourg: European Commission*, 2020, 1–244.

[6] C. Liu, B. C. Colón, M. Ziesack, P. A. Silver and D. G. Nocera, Water splitting–biosynthetic system with CO_2 reduction efficiencies exceeding photosynthesis, *Science*, 2016, **352**, 1210–1213, DOI: 10.1126/science.aaf5039.

[7] E. P. Komarala, A. A. Alkhoori, X. Zhang, H.-M. Cheng and K. Polychronopoulou, Design and synthesis of thermally stable single atom catalysts for thermochemical CO2 reduction, *Journal of Energy Chemistry*, 2023, **86**, 246–262, DOI: 10.1016/j.jechem.2023.07.032.

[8] J. Wu, Y. Huang, W. Ye and Y. Li, CO_2 reduction: from the electrochemical to photochemical approach, *Advanced Science*, 2017, **4**, 1700194, DOI: 10.1002/advs.201700194.

[9] D. S. Laitar, P. Müller and J. P. Sadighi, Efficient Homogeneous Catalysis in the Reduction of CO2 to CO, *Journal of the American Chemical Society*, 2005, **127**, 17196–17197, DOI: 10.1021/ja0566679.

[10] P. Yaashikaa, P. S. Kumar, S. J. Varjani and A. Saravanan, A review on photochemical, biochemical and electrochemical transformation of CO2 into value-added products, *J. CO2 Util.*, 2019, **33**, 131–147, DOI: 10.1016/j.jcou.2019.05.017.

[11] K. P. Kuhl, E. R. Cave, D. N. Abram and T. F. Jaramillo, New Insights Into the Electrochemical Reduction of Carbon Dioxide on Metallic Copper Surfaces, *Energy Environ. Sci.*, 2012, **5**, 7050, DOI: 10.1039/c2ee21234j.

[12] A. A. Peterson and J. K. Nørskov, Activity Descriptors for CO_2 Electroreduction to Methane on Transition-metal Catalysts, *J. Phys. Chem. Lett.*, 2012, **3**, 251–258, DOI: 10.1021/jz201461p.

[13] K. An and G. A. Somorjai, Size and shape control of metal nanoparticles for reaction selectivity in catalysis, *ChemCatChem*, 2012, **4**, 1512–1524, DOI: 10.1002/cctc.201200229.

[14] T. W. van Deelen, C. Hernández Mejía and K. P. de Jong, Control of metal-support interactions in heterogeneous catalysts to enhance activity and selectivity, *Nature Catalysis*, 2019, **2**, 955–970, DOI: 10.1038/s41929-019-0364-x.

[15] F. Zaera, Designing sites in heterogeneous catalysis: are we reaching selectivities competitive with those of homogeneous catalysts?, *Chemical Reviews*, 2022, **122**, 8594–8757, DOI: 10.1021/acs.chemrev.1c00905.

[16] D. Liu, Q. He, S. Ding and L. Song, Structural regulation and support coupling effect of single-atom catalysts for heterogeneous catalysis, *Advanced Energy Materials*, 2020, **10**, 2001482, DOI: 10.1002/aenm.202001482.

[17] Y. Wang, Z. Chen, P. Han, Y. Du, Z. Gu, X. Xu and G. Zheng, Single-atomic Cu with multiple oxygen vacancies on ceria for electrocatalytic CO2 reduction to CH4, *ACS Catal.*, 2018, **8**, 7113–7119, DOI: 10.1021/acscatal.8b01014.

[18] X. Zhu, J. Huang and M. Eikerling, Electrochemical CO_2 Reduction at Silver from a Local Perspective, *ACS Catal.*, 2021, **11**, 14521–14532, DOI: 10.1021/acscatal.1c04791.

[19] A. Rendon-Calle, S. Builes and F. Calle-Vallejo, A brief review of the computational modeling of CO2 electroreduction on Cu electrodes, *Current Opinion in Electrochemistry*, 2018, **9**, 158–165.

[20] D. Y. Jo, H. C. Ham and K.-Y. Lee, Facet-dependent Electrocatalysis in the HCOOH Synthesis From CO_2 Reduction on Cu Catalyst: A Density Functional Theory Study, *Appl. Surf. Sci.*, 2020, **527**, 146857, DOI: 10.1016/j.apsusc.2020.146857.

[21] L. G. Verga, P. C. D. Mendes, V. K. Ocampo-Restrepo and J. L. F. Da Silva, the Role of Site Coordination on the CO_2 Electroreduction Pathway on Stepped and Defective Copper Surfaces, *Catal. Sci. Technol.*, 2021, **11**, 2770–2781, DOI: 10.1039/d0cy02337j.

[22] B. Hammer, Reactivity of a Stepped Surface NO Dissociation on Pd(211), *Faraday Discuss.*, 1998, **110**, 323–333, DOI: 10.1039/A801126E.

[23] G. Füĉchsle, ü. E. Kun Cao and, E. W. Smeets, A. W. Kleyn, L. B. Juurlink and G.-J. Kroes, Anomalous Dependence of the Reactivity on the Presence of Steps: Dissociation of D2 on Cu(211), *J. Phys. Chem. Lett.*, 2018, **9**, 170–175, DOI: 10.1021/acs.jpclett.7b03097.

[24] F. Jalid, T. S. Khan, F. Q. Mir and M. A. Haider, Understanding Trends in Hydrodeoxygenation Reactivity of Metal and Bimetallic Alloy Catalysts from Ethanol Reaction on Stepped Surface, *J. Catal.*, 2017, **353**, 265–273, DOI: 10.1016/j.jcat.2017.07.018.

[25] K. Gu, F. Wei, Y. Cai, S. Lin and H. Guo, Dynamics of Initial Hydrogen Spillover from a Single Atom Platinum Active Site to the Cu(111) Host Surface: The Impact of Substrate Electron–Hole Pairs, *J. Phys. Chem. Lett.*, 2021, **12**, 8423–8429, DOI: 10.1021/acs.jpclett.1c02019.

[26] K. Yang and B. Yang, Identification of the Active and Selective Sites Over a Single Pt Atom-alloyed Cu Catalyst for the Hydrogenation of 1,3-butadiene: a Combined DFT and Microkinetic Modeling Study, *J. Phys. Chem. C*, 2018, **122**, 10883–10891, DOI: 10.1021/acs.jpcc.8b01980.

[27] R. Réocreux, M. Uhlman, T. Thuening, P. Kress, R. Hannagan, M. Stamatakis and E. C. H. Sykes, Efficient and Selective Carbon–Carbon Coupling on Coke-Resistant PdAu Single-Atom Alloys, *Chem. Comm.*, 2019, **55**, 15085–15088, DOI: 10.1039/C9CC07932G.

[28] S. Hasegawa, S. Takano, S. Yamazoe and T. Tsukuda, Prominent Hydrogenation Catalysis of a PVP-stabilized Au_{34} Superatom Provided by Doping a Single Rh Atom, *Chem. Comm.*, 2018, **54**, 5915–5918, DOI: 10.1039/C8CC03123A.

[29] N. Cheng, S. Stambula, D. Wang, M. N. Banis, J. Liu, A. Riese, B. Xiao, R. Li, T.-K. Sham, L.-M. Liu *et al.*, Platinum Single-Atom and Cluster Catalysis of the Hydrogen Evolution Reaction, *Nat. Commun.*, 2016, **7**, 1–9, DOI: 10.1038/ncomms13638.

[30] M. T. Darby, R. Réocreun, E. C. H. Sykes, A. Michaelides and M. Stamatakis, Elucidating the Stability and Reactivity of Surface Intermediates on Single-Atom Alloy Catalysts, *ACS Catal.*, 2018, **8**, 5038–5050, DOI: 10.1021/acscatal.8b00881.

[31] G. Kyriakou, M. B. Boucher, A. D. Jewell, E. A. Lewis, T. J. Lawton, A. E. Baber, H. L. Tierney, M. Flytzani-Stephanopoulos and E. C. H. Sykes, Isolated Metal Atom

Geometries as a Strategy for Selective Heterogeneous Hydrogenations, *Science*, 2012, **335**, 1209–1212, DOI: 10.1126/science.1215864.

[32] M. D. Marcinkowski, A. D. Jewell, M. Stamatakis, M. B. Boucher, E. A. Lewis, C. J. Murphy, G. Kyriakou and E. C. H. Sykes, Controlling a spillover pathway with the molecular cork effect, *Nat. Mater.*, 2013, **12**, 523–528, DOI: 10.1038/nmat3620.

[33] Z. Tian, C. Priest and L. Chen, Recent progress in the theoretical investigation of electrocatalytic reduction of CO_2, *Advanced Theory and Simulations*, 2018, **1**, 1800004.

[34] Q. Li, Y. Ouyang, S. Lu, X. Bai, Y. Zhang, L. Shi, C. Ling and J. Wang, Perspective on theoretical methods and modeling relating to electro-catalysis processes, *Chemical Communications*, 2020, **56**, 9937–9949.

[35] J. K. Nørskov, T. Bligaard, J. Rossmeisl and C. H. Christensen, Towards the Computational Design of Solid Catalysts, *Nat. Chem.*, 2009, **1**, 37–46.

[36] D. J. Griffiths and D. F. Schroeter, *Introduction to quantum mechanics*, Cambridge University Press, 2018.

[37] W. Koch and M. C. Holthausen, *A chemist's guide to density functional theory*, John Wiley & Sons, 2015.

[38] P. Hohenberg and W. Kohn, Inhomogeneous electron gas, *Physical review*, 1964, **136**, B864.

[39] F. Jensen, *Introduction to Computational Chemistry*, Wiley, Chichester, 1999.

[40] J. P. Perdew, K. Burke and M. Ernzerhof, Generalized gradient approximation made simple, *Physical review letters*, 1996, **77**, 3865.

[41] J. K. Nørskov, J. Rossmeisl, A. Logadottir, L. Lindqvist, J. R. Kitchin, T. Bligaard and H. Jonsson, Origin of the overpotential for oxygen reduction at a fuel-cell cathode, *The Journal of Physical Chemistry B*, 2004, **108**, 17886–17892, DOI: 10.1021/jp047349j.

[42] A. A. Peterson, F. Abild-Pedersen, F. Studt, J. Rossmeisl and J. K. Nørskov, How copper catalyzes the electroreduction of carbon dioxide into hydrocarbon fuels, *Energy Environ. Sci*, 2010, **3**, 1311–1315, DOI: 10.1039/C0EE00071J.

[43] A. Rendón-Calle, S. Builes and F. Calle-Vallejo, Substantial improvement of electrocatalytic predictions by systematic assessment of solvent effects on adsorption energies, *Applied Catalysis B: Environmental*, 2020, **276**, 119147, DOI: 10.1016/j.apcatb.2020.119147.

[44] A. H. Larsen, J. J. Mortensen, J. Blomqvist, I. E. Castelli, R. Christensen, M. Dułak, J. Friis, M. N. Groves, B. Hammer, C. Hargus *et al.*, The atomic simulation environment—a Python library for working with atoms, *J. Condens. Matter Phys.*, 2017, **29**, 273002, DOI: 10.1088/1361-648X/aa680e.

[45] M. T. Tang, H. Peng, P. S. Lamoureux, M. Bajdich and F. Abild-Pedersen, From Electricity to Fuels: Descriptors for C1 Selectivity in Electrochemical CO_2 Reduction, *Appl. Catal. B: Environ.*, 2020, **279**, 119384, DOI: 10.1016/j.apcatb.2020.119384.

[46] Y. Hori, H. Wakebe, T. Tsukamoto and O. Koga, Electrocatalytic Process of CO Selectivity in Electrochemical Reduction of CO_2 at Metal Electrodes in Aqueous Media, *Electrochim. Acta*, 1994, **39**, 1833–1839, DOI: 10.1016/0013-4686(94)85172-7.

[47] X.-G. Zhang, X. Jin, D.-Y. Wu and Z.-Q. Tian, Selective Electrocatalytic Mechanism of CO_2 Reduction Reaction to CO on Silver Electrodes: a Unique Reaction Intermediate, *J. Phys. Chem. C*, 2018, **122**, 25447–25455, DOI: 10.1021/acs.jpcc.8b08170.

[48] G. Kresse and J. Hafner, *Ab initio* Molecular Dynamics for Open-shell Transition Metals, *Phys. Rev. B*, 1993, **48**, 13115–13118, DOI: 10.1103/physrevb.48.13115.

[49] G. Kresse and J. Furthmüller, Efficient Iterative Schemes Forab Initiototal-energy Calculations Using a Plane-wave Basis set, *Phys. Rev. B*, 1996, **54**, 11169–11186, DOI: 10.1103/physrevb.54.11169.

[50] G. Kresse and D. Joubert, From Ultrasoft Pseudopotentials to the Projector Augmented-wave Method, *Phys. Rev. B*, 1999, **59**, 1758–1775, DOI: 10.1103/physrevb.59.1758.

[51] J. P. Perdew, K. Burke and M. Ernzerhof, Generalized Gradient Approximation Made Simple, *Phys. Rev. Lett.*, 1996, **77**, 3865–3868, DOI: 10.1103/physrevlett.77.3865.

[52] P. E. Blöchl, Projector Augmented-Wave Method, *Phys. Rev. B*, 1994, **50**, 17953–17979, DOI: 10.1103/physrevb.50.17953.

[53] S. Grimme, J. Antony, S. Ehrlich and H. Krieg, A Consistent and Accurate ab Initio Parametrization of Density Functional Dispersion Correction (DFT-D) for the 94 Elements H–Pu, *J. Chem. Phys.*, 2010, **132**, 154104, DOI: 10.1063/1.3382344.

[54] R. L. H. Freire, D. Guedes-Sobrinho, A. Kiejna and J. L. F. Da Silva, Comparison of the Performance of van der Waals Dispersion Functionals in the Description of Water and Ethanol on Transition Metal Surfaces, *J. Phys. Chem. C*, 2018, **122**, 1577–1588, DOI: 10.1021/acs.jpcc.7b09749.

[55] K. E. A. Batista, V. K. Ocampo-Restrepo, M. D. Soares, M. G. Quiles, M. J. Piotrowski and J. L. F. Da Silva, *Ab initio* Investigation of CO_2 Adsorption

on 13-atom 4*d* Clusters, *J. Chem. Inf. Model.*, 2020, **60**, 537–545, DOI: 10.1021/acs.jcim.9b00792.

[56] S. Ehrlich, J. Moellmann, W. Reckien, T. Bredow and S. Grimme, System-Dependent Dispersion Coefficients for the DFT-D3 Treatment of Adsorption Processes on Ionic Surfaces, *ChemPhysChem*, 2011, **12**, 3414–3420, DOI: 10.1002/cphc.201100521.

[57] N.-X. Qiu, Y. Xue, Y. Guo, W.-J. Sun and W. Chu, Adsorption of Methane on Carbon Models of Coal Surface Studied by the Density Functional Theory Including Dispersion Correction (DFT-D3), *Comput. Theor. Chem.*, 2012, **992**, 37–47, DOI: 10.1016/j.comptc.2012.04.024.

[58] P. Tereshchuk, R. C. Amaral, Y. Seminovski and J. L. F. Da Silva, Glycerol Adsorption on a Defected Pt_6/Pt(100) Substrate: A Density Functional Theory Investigation Within the D3 van der Waals Correction, *RSC Adv.*, 2017, **7**, 17122–17127, DOI: 10.1039/c7ra00976c.

[59] U. S. Shenoy and D. K. Bhat, Electronic Structure Engineering of $SrTiO_3$ Via Rhodium Doping: A DFT Study, *J. Phys. Chem. Solids*, 2021, **148**, 109708, DOI: 10.1016/j.jpcs.2020.109708.

[60] Z. Zhang, A. Kladi and X. E. Verykios, Effects of Carrier Doping on Kinetic Parameters of CO_2 Hydrogenation on Supported Rhodium Catalysts, *J. Catal.*, 1994, **148**, 737–747, DOI: 10.1006/jcat.1994.1260.

[61] S. Durukanog-Tildelu, A. Kara and T. S. Rahman, Local Structural and Vibrational Properties of Stepped Surfaces: Cu(211), Cu(511), and Cu(331), *Phys. Rev. B*, 1997, **55**, 13894, DOI: 10.1103/PhysRevB.55.13894.

[62] Q.-L. Tang and Z.-X. Chen, Density Functional Slab Model Studies of Water Adsorption on Flat and Stepped Cu Surfaces, *Surf. Sci.*, 2007, **601**, 954–964, DOI: 10.1016/j.susc.2006.11.036.

[63] R. Hoppe, Effective Coordination Numbers (ECoN) and Mean Active Fictive Ionic Radii (MEFIR), *Z. Kristallogr.*, 1979, **150**, 23–52, DOI: 10.1524/zkri.1979.150.1-4.23.

[64] J. L. F. Da Silva, Effective Coordination Concept Applied for Phase Change $(GeTe)_m(Sb_2Te_3)_n$ Compounds, *J. Appl. Phys.*, 2011, **109**, 023502, DOI: 10.1063/1.3533422.

[65] R. V. de Amorim, K. E. Batista, G. R. Nagurniak, R. P. Orenha, R. L. Parreira and M. J. Piotrowski, CO, NO, and SO Adsorption on Ni Nanoclusters: a DFT Investigation, *Dalton Trans.*, 2020, **49**, 6407–6417, DOI: 10.1039/D0DT00288G.

[66] L. G. Verga, P. C. D. Mendes, V. K. Ocampo-Restrepo and J. L. F. Da Silva, The Role of Site Coordination on the CO2 Electroreduction Pathway on Stepped

and Defective Copper Surfaces, *Catal. Sci. Technol.*, 2021, **11**, 2770–2781, DOI: 10.1039/d0cy02337j.

[67] R. Hoppe, the Coordination Number–an "Inorganic Chameleon", *Angew. Chem., Int. Ed. Engl.*, 1970, **9**, 25–34, DOI: 10.1002/anie.197000251.

[68] J. Hölzl and F. K. Schulte, Work function of metals, *Solid State Phys.*, 2006, 1–150, DOI: 10.1007/BFb0048919.

[69] M. Yu and D. R. Trinkle, Accurate and efficient algorithm for Bader charge integration, *J. Chem. Phys.*, 2011, **134**, year, DOI: 10.1063/1.3553716.

[70] G. Henkelman, A. Arnaldsson and H. Jónsson, A Fast and Robust Algorithm for Bader Decomposition of Charge Density, *Comput. Mater. Sci.*, 2006, **36**, 354–360.

[71] P. Linstrom and W. Mallard, *NIST Chemistry WebBook, NIST Standard Reference Database*, National Institute of Standards and Technology, 2022, DOI: 10.18434/T4D303.

[72] J. Paier, R. Hirschl, M. Marsman and G. Kresse, author, *J. Chem. Phys.*, 2005, **122**, 234102.

[73] J. W. HAN, J. R. KITCHIN and D. S. SHOLL, Step Decoration of Chiral Metal Surfaces, *Chem. Phys.*, 2009, **130**, 124710, DOI: 10.1063/1.3096964.

[74] N. Ferri, R. A. DiStasio Jr, A. Ambrosetti, R. Car and A. Tkatchenko, Electronic Properties of Molecules and Surfaces with a Self-Consistent Interatomic van der Waals Density Functional, *Physical review letters*, 2015, **114**, 176802, DOI: 10.1103/PhysRevLett.114.176802.

[75] Y. Jiang, J. Li, G. Su, N. Ferri, W. Liu and A. Tkatchenko, Tuning the Work Function of Stepped Metal Surfaces by Adsorption of Organic Molecules, *J. Phys.: Condens. Matter*, 2017, **29**, 204001, DOI: 10.1088/1361-648X/aa693e.

[76] W. M. Haynes, *CRC Handbook of Chemistry and Physics*, CRC press, 2014.

[77] H. Thirumalai and J. R. Kitchin, Investigating the Reactivity of Single Atom Alloys Using Density Functional Theory, *Top. Catal.*, 2018, **61**, 462–474, DOI: 10.1007/s11244-018-0899-0.

[78] M. T. Greiner, T. Jones, S. Beeg, L. Zwiener, M. Scherzer, F. Girgsdies, S. Piccinin, M. Armbrüster, A. Knop-Gericke and R. Schlögl, Free-atom-like d States in Single-Atom Alloy Catalysts, *Nat. Chem.*, 2018, **10**, 1008–1015, DOI: 10.1038/s41557-018-0125-5.

[79] A. A. Peterson and J. K. Nørskov, Activity Descriptors for CO_2 Electroreduction to Methane on Transition-Metal Catalysts, *J. Phys. Chem. Lett.*, 2012, **3**, 251–258, DOI: 10.1021/jz201461p.

[80] T. D. Spivey and A. Holewinski, Selective interactions between free-atom-like d-states in single-atom alloy catalysts and near-frontier molecular orbitals, *J. Am. Chem. Soc.*, 2021, **143**, 11897–11902, DOI: 10.1021/jacs.1c04234.

[81] S. Guo, Y. Li, L. Liu, L. Liu, X. Zhang and S. Zhang, Computational identification of a new adsorption site of CO_2 on the Ag (211) surface, *ChemistrySelect*, 2020, **5**, 11503–11509, DOI: 10.1002/slct.202003149.

[82] M. Mavrikakis, B. Hammer and J. K. Nørskov, Effect of strain on the reactivity of metal surfaces, *Phys. Rev. Lett.*, 1998, **81**, 2819, DOI: 10.1103/PhysRevLett.81.2819.

[83] P. Liu and J. K. Nørskov, Ligand and ensemble effects in adsorption on alloy surfaces, *Phys. Chem. Chem. Phys.*, 2001, **3**, 3814–3818, DOI: 10.1039/B103525H.

[84] M. M. Neto, L. G. Verga, J. L. Da Silva and B. R. Galvão, The role of single-atom Rh-dopants in the adsorption properties of OH and CO on stepped Ag (211) surfaces, *PCCP*, 2023, **25**, 4939–4949, DOI: 10.1039/D2CP04376A.

[85] M. Karamad, V. Tripkovic and J. Rossmeisl, Intermetallic Alloys as CO Electroreduction Catalysts Role of Isolated Active Sites, *ACS Catal.*, 2014, **4**, 2268–2273, DOI: 10.1021/cs500328c.

[86] M.-J. Cheng, E. L. Clark, H. H. Pham, A. T. Bell and M. Head-Gordon, Quantum mechanical screening of single-atom bimetallic alloys for the selective reduction of CO_2 to C1 hydrocarbons, *ACS Catal.*, 2016, **6**, 7769–7777, DOI: 10.1021/acscatal.6b01393.

[87] Y. Feng, W. An, Z. Wang, Y. Wang, Y. Men and Y. Du, Electrochemical CO_2 Reduction Reaction on MCu(211) Bimetallic Single-atom Surface Alloys: Mechanism, Kinetics, and Catalyst Screening, *ACS Sustainable Chem. Eng.*, 2019, **8**, 210–222, DOI: 10.1021/acssuschemeng.9b05183.